OPTICAL BIOPSY INSTRUMENT DESIGN AND DATA ANALYSIS

OPTICAL BIOPSY INSTRUMENT DESIGN AND PARAMETER EXTRACTION FROM HYPERSPECTRAL TIME-RESOLVED FLUORESCENCE DATA

By FARES BADR, B. ENG

A Thesis Submitted to the School of Biomedical Engineering in Partial Fulfillment of the Requirements for the Degree Master of Applied Science

MASTER OF APPLIED SCIENCE (2019) McMaster University

School of Biomedical Engineering Hamilton, Ontario

TITLE: Optical Biopsy Instrument Design and Parameter Extraction from Hyperspectral Time-resolved Fluorescence Data

AUTHOR: Fares Badr,

B.Eng (McMaster University)

SUPERVISOR: Professor Qiyin Fang

NUMBER OF PAGES: xi, 56

Abstract

Complete resection is correlated to better patient outcome in aggressive cancers such as glioblastoma. Optical biopsy refers to a family of techniques utilizing optical properties of living targets to make diagnoses where a biopsy would conventionally be used. Such a technology can potentially guide neurosurgeons in removing glioblastomas.

Diffuse reflectance (DR) and Time-resolved fluorescence (TRF) have previously been investigated for their ability to measure biomarkers indicative of cancer. One of the difficulties faced in using TRF as a diagnostic tool is that multiple endogenous fluorophores will simultaneously contribute to the signal. This makes it difficult to attribute fluorescence lifetimes or spectral changes to one type of molecule in the tissue.

This thesis focuses on the challenge of separating the components in a TRF measurement and their fractional contributions. A DR-TRF instrument was designed and built and characterized using fluorescent dyes. An orthonormal basis deconvolution method combined with a Fourier-domain method were tested for their ability to unmix fluorescent components in a hyperspectral TRF measurement. This method was tested on dye mixtures and retrieved fluorescence lifetimes of 4.6±0.4 ns and 2.7±0.2 ns in a mixture of Fluorescein and Coumarin-6 at concentrations of 5 μM each. It was also tested on an *ex-vivo* brain tissue where the fluorescence was approximated as a sum of 2 components.

Acknowledgements

I would like to thank my supervisor, Dr. Qiyin Fang, for his guidance and insights and freedom to focus on questions that interested me.

I also want to extend my thanks to the members of the Biophotonics research group for their useful discussions when I ran into troubles.

I want to thank Oscar Yeung for his efforts in the design and assembly of the acquisition instrument.

Thanks to Dr. John Provias for explaining some of the difficulties faced in neuropathology which motivated the research, and thanks to Dr. Naresh Murty for his cooperation in the brain optical biopsy study.

I also thank my family for their moral support.

Table of Contents

List of Figures and Tables

List of Abbreviations

9CA:	9-Cyanoanthracene
AOTF:	Acousto-optical Tunable Filter
C6:	Coumarin-6
CMM:	Center-of-Mass Method
DR:	Diffuse Reflectance
DRS:	Diffuse Reflectance Spectroscopy
FAD:	Flavin Adenine dinucleotide
FD:	Frequency Domain
FL:	Fluorescein
FLIM:	Fluorescence Lifetime Imaging Microscopy
FPGA:	Field-Programmable Gate Array
GSPS:	Giga-Samples Per Second
HGG:	High-Grade Glioma
ICCD:	Intensified Charge-Coupled Device
IRF:	Instrument Response Function
LCTF:	Liquid Crystal Tunable Filter
LM:	Levenberg-Marquardt algorithm
LUT:	Look-Up Table
MCP-PMT:	Microchannel Plate Photomultiplier Tube
NA:	Numerical Aperture
NADH:	Reduced Nicotinamide adenine dinucleotide
Nd:YAG:	Neodymium-doped Yttrium Aluminum Garnet
PMT:	Photomultiplier Tube
RF:	Radio Frequency
RLD:	Rapid Lifetime Determination
SDD:	Source-Detector Distance
TCSPC:	Time Correlated Single Photon Counting
TRF:	Time Resolved Fluorescence

List of Symbols

$\hat{\boldsymbol{s}}$	Unit direction vector
$P(\theta)$	Phase function
$L(\boldsymbol{r}, \hat{\boldsymbol{s}})$	Irradiance
μ_s	Scattering coefficient
μ_a	Absorption coefficient
μ_t	Transport coefficient
g	Anisotropy coefficient
$I(t)$	Intensity
τ	Fluorescence lifetime
k_i	Non-radiative transition rate
k_e	Radiative transition rate
$\boldsymbol{H}$	Hessian matrix
$\boldsymbol{g}$	gradient vector
$\boldsymbol{w}$	Parameters vector
α	Laguerre scale factor
L	Laguerre order
$G(\omega)$	Real component of phasor
$S(\omega)$	Complex component of phasor
f_i	Fractional contribution
$h(t)$	Intrinsic fluorescence decay
$y(t)$	Measured fluorescence decay
$x(t)$	Instrument response function
b_j	Laguerre function of order j
v_j	Convolution of Laguerre function with IRF
N	Number of samples
m	mass
$S(\lambda)$	Sensitivity
σ	Noise
$\%C$	Relative photon contribution

Chapter 1

Introduction

1.1. Optical Biopsy

A biopsy is a procedure where tissue is removed from the body and investigated for the presence of a disease. Biopsies on tumors provide a diagnosis with the grade of the tumor, its invasiveness and the type of cancer present. Biopsies are subject to large sampling error, because only a limited volume of tissue can be extracted depending on the target organ. Additionally, biopsies do not give real time information, since the sample must be sliced, fixed, stained and looked at by a pathologist. This process typically takes a few days from the removal of tissue to diagnosis. Biopsies also carry a risk of haemorrhages and organ damage [1]. To overcome these problems, optical biopsy has been the target of research as a possible solution.

Optical biopsy refers to the use of optical techniques, such as imaging and spectroscopy, to provide diagnostic information. This can be achieved by optically detecting biomarkers indicating that a tissue is cancerous. Optical biopsy can potentially overcome the sampling error issues of conventional biopsy, since a large area of tissue can be investigated in a short time frame. Additionally, there is a reduced risk of hemorrhages and it avoids the unwanted side effects of removing tissue from vital organs. Brain cancer is one of the target applications of optical biopsy. Difficulties in brain cancer include the invasiveness of the cancer, particularly of glioblastomas, which makes sampling large areas necessary for complete excision. More complete removal of the cancer is correlated to lower probability of local recurrence, which correlates with longer patient survival [4]. Another target application is optical biopsy for breast cancer.

Our lab group has investigated diffuse reflectance (DR) and time resolved fluorescence (TRF) for optical biopsy. Autofluorescence gives information about the metabolic activity of the cells. This has shown potential in optically identifying glioblastoma cells [5]. Diffuse reflectance can be used to find changes in water, lipid, and haemoglobin content in the tissue [6]. Additionally, neoplasia or dysplasia can cause differences in reflectance properties of cancerous tissue compared to normal tissue [7].

The idea behind integrating the DR and TRF modalities is that they provide increased contrast compared with having a single modality. Additionally, the two sets of measurements complement each other since the tissue's optical transport properties affect the measured fluorescence. Thus, if the absorption and scattering properties are known, the measured fluorescence can be corrected to provide intrinsic fluorescence information.

1.2. Challenges

Developing an optical biopsy technology based on DR-TRF comes with several challenges. Data acquisition challenges lie in collecting the TRF signal, since the expected emission intensity from endogenous fluorophores is weak. Another acquisition challenge is integrating the DR and TRF components such that they probe the same volume of tissue.

The next set of challenges arise in data processing. In optical biopsy studies, it is typical to use linear discriminant analysis to demonstrate differences between cancerous and healthy tissue. However, for data interpretation and reproducibility, it is desirable to process the raw data into a few parameters that are related to physical properties such as increase in concentration or local pH. This will allow for explanations of statistical differences between different types of tissue. For the TRF data, this may involve quantifying the measured spectra and decays in terms of the presence of individual fluorophores and their relative contributions and deviations in their emission spectra and lifetimes. For the DR data, the processing may involve translating the reflectance measurements into absorption and scattering coefficients as a function of wavelength.

Another challenge exists in building a database of DR-TRF measurements from cancerous and non-cancerous tissue. The number of patients from each target group should be large enough to have statistically significant results. Additionally, there is the challenge of co-registration. That is making sure that the volume that was probed for DR-TRF measurement is the same volume that the pathologist provided a classification for. This is particularly important for important for invasive tumors such as glioblastomas, where the biopsy tissue may be a mixture of healthy and cancerous cells.

1.3. Overview

Chapter 2 provides the background for diffuse reflectance and time-resolved fluorescence. This includes models used to describe light transport in tissue and fluorescence decays. Additionally, it presents the background for detectors and optical components used in the rest of this thesis, as well as common data analysis methods for time resolved fluorescence.

Chapter 3 relates to building an instrument for a DR-TRF study. A DR-TRF instrument has been built and characterized previously [2], and will be referred to as system A. A new DR-TRF instrument, referred to as system B, was built and presented in chapter 3. System B is an improvement over system A in regard to collection efficiency and sampling rate. Chapter 3 addresses the challenges faced in data acquisition, the design choices for system B and a verification of its ability to measure fluorescence lifetimes.

Chapter 4 addresses the challenges in data processing of the TRF data. One of the problems with analyzing biological TRF data is the choice of model to describe the data. One approach that has previously been tested is Laguerre deconvolution, where a model-free fit is used to deconvolve and describe the data with a few parameters. Chapter 4 contains a simulation aimed at finding the expected error in deconvolving the intrinsic

fluorescence from the instrument response using Laguerre deconvolution. Additionally, it tackles the problem of separating a measurement of a mixture of fluorophores into individual components. Phasor analysis as well as a Gaussian-mixture model are tested for their ability to unmix individual lifetimes from hyperspectral TRF data.

Chapter 5 applies the acquisition and processing of previous chapters to cancerous brain tissue. This chapter concludes with the challenges that remain to make this a conclusive optical biopsy study.

1.4. Contributions

The contributions of this thesis to optical biopsy research are outlined below:

- Designed, built and characterized a new DR-TRF instrument (System B).

- Based on system B's design, improved an existing DR-TRF instrument (System A).

- Investigated component unmixing in biological tissue using Laguerre deconvolution and phasor analysis on hyperspectral TRF data.

- Investigated Gaussian-Mixture models for representing hyperspectral TRF data.

- Acquired DR-TRF measurements of a glioblastoma tissue and used it to test TRF analysis methods on endogenous fluorophores.

Chapter 2

Background

Diffuse reflectance spectroscopy (DRS) and time-resolved fluorescence (TRF) operate on the principle that light can interact with tissue, giving information about the tissue's absorption, scattering and fluorescent properties. This chapter presents an overview of those interactions specifically relevant to the DRS and TRF instrument and cover different methods to measure parameters related to those phenomena. Algorithms used to analyze DRS and TRF data are briefly explained.

2.1. Light Interaction with Tissue

The path of light through biological tissue is described by the electromagnetic wave model of light, which obeys Maxwell's equations. However, tissue is a turbid medium, so light wave-fronts travelling through it cross many interfaces of changing refractive indices. Each interface may induce partial reflection and refraction. The physical and mathematical complexity of this scenario makes an analytical solution of Maxwell's equations challenging. A more commonly used model for predicting the path of light is based on transport theory, where the absorption coefficient, scattering coefficient, and phase function determine the irradiance on a given area [8,9].

$$\hat{\boldsymbol{s}} \cdot \nabla L(\boldsymbol{r}, \hat{\boldsymbol{s}}) + \mu_t L(\boldsymbol{r}, \hat{\boldsymbol{s}}) = \frac{\mu_t}{4\pi} \int_0^{4\pi} P(\boldsymbol{s}, \hat{\boldsymbol{s}})\, L(\boldsymbol{r}, \hat{s})\, d\Omega + Source \qquad \textbf{(2.1)}$$

L is the irradiance at point $\boldsymbol{r}$, in direction $\hat{\boldsymbol{s}}$ (unit direction vector) and μ_t is the transport coefficient, defined as the sum of absorption and scattering coefficients. P is the phase function, which gives the probability that light travelling in a direction $\boldsymbol{s}$ will scatter within a solid angle $d\Omega$. The absorption and scattering coefficients (μ_a / μ_s; cm $^{-1}$) are the inverse of the average distances a photon travels without being absorbed or scattered respectively.

In turbid media, absorption arises from the presence of chromophores. For example, in biological tissue, one of the main absorbers is blood, due to its hemoglobin content, which has an absorption coefficient >100cm^{-1} for blue light, and this drops to roughly 1-10 cm^{-1} for red light. Water and fat have low absorption in the visible range (<0.1 cm^{-1}), which increases to above 1 cm^{-1} in the infrared regime [10]. Scattering refers to a change in direction, possibly due to interaction with particles of similar dimensions to the wavelength (Mie scattering) or a series of reflections and refractions at non-parallel planes or interaction with particles smaller than the wavelength of light (Rayleigh scattering). The scattering coefficient also has a unit of cm $^{-1}$, such that the un-scattered intensity of light after a distance L is:

$$I = I_0 e^{-\mu_s L} \quad \textbf{(2.2)}$$

The phase function gives the directionality of scattering. A commonly used phase function when scattering particles are randomly distributed is the Henyey-Greenstein phase function, which gives the fraction of photons scattered at an angle θ from the forward ray [11].

$$P(\theta) = \frac{\mu_s}{4\pi\,\mu_t} \frac{1-g^2}{(1+g^2-2g\cos\theta)^{\frac{3}{2}}} \quad \textbf{(2.3)}$$

Here, g is the anisotropy coefficient, a number from -1 to +1, defined as $g = < cos\theta >$. An anisotropy coefficient of +1 means that the scattering is entirely in the forward direction, while a value of 0 means that the scattering is isotropic. Sources of Rayleigh scattering in tissue are sub-micron structures such as mitochondria and lysosomes. Collagen fibrils also contribute to scattering, which is affected by the dimensions and spacing of the fibrils [12,13,14].

Besides the transport of light in tissue, an optical interaction of interest is fluorescence. Fluorescence is a phenomenon explained in a quantum mechanical framework as follows: A photon is absorbed, exciting an electron to a higher energy state of the same spin (singlet state), and then a photon is emitted if the electron de-excites radiatively. This process is illustrated in a Jablonski diagram, which shows the possible energy levels of a molecule.

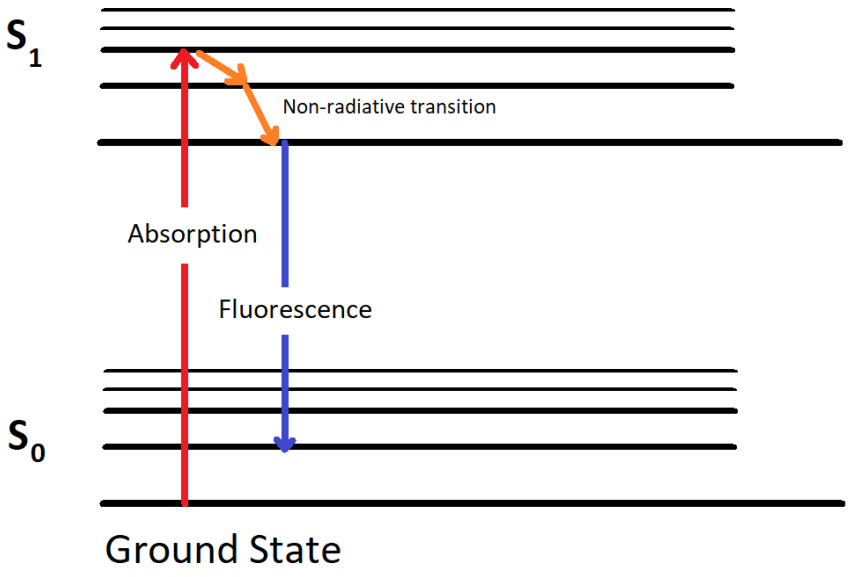

Figure 2-1. Jablonski diagram showing possible energy states in a fluorescent molecule

In this model, electrons spend time in the excited state, with a fixed probability of depopulation in a given time. The equation describing this behavior is:

$$\frac{dN}{dt} = -N(k_i + k_e) + \alpha \quad \textbf{(2.4)}$$

Where k_i and k_e are rates of non-radiative and radiative transitions respectively, and α is the rate at which electrons are excited from the ground state. Assuming that no more electrons are being excited ($\alpha = 0$), the decay of fluorescence intensity is given by:

$$I(t) = I_0 e^{-\frac{t}{\tau}} \quad \textbf{(2.5)}$$

τ is referred to as the fluorescence lifetime and is related to the transition rates by equation 2.6.

$$\tau = \frac{1}{k_i + k_e} \quad \textbf{(2.6)}$$

The fluorescence lifetime is independent of the intensity of emission. However, it is affected by the fluorophore's micro-environment. The fluorescence spectrum (intensity as a function of wavelength) and lifetime are determined by the molecule's chemistry and its functional groups which determine its electronic structure. Factors that affect the fluorescence lifetime include pH, conformation (molecule shape), temperature and solvent effects [15,16,17,18].

Fluorophores present naturally in biological tissue are called endogenous fluorophores. Examples are amino acids, enzyme co-factors, structural proteins, and lipids. Amino acids such as tryptophan and tyrosine have excitation peaks below 300 nm. NADH and NADPH are enzyme co-factors with NADPH catalyzing anabolic reactions and NADH being involved in catabolic reactions that produce ATP [19]. These two co-factors have identical fluorescence spectra, with absorption peaks at 340 nm and emission peaks at 460 nm. Thus, they are sometimes lumped together in spectroscopic measurements as NAD(P)H. However, since the fluorescence lifetime is affected by protein binding, and these co-enzymes bind to different sets of proteins, they can be differentiated based on their fluorescence lifetime [20].

Collagens and Elastin fluoresce with absorptions peaks around 340 nm, and FAD has multiple absorption peaks. Fluorescence lifetimes vary greatly depending on the environment and may not always follow the exponential model shown above. They are generally in the range of <10 ps to 6 ns [21].

2.2. Measuring Optical Properties of Tissue

2.2.1. Absorption and Scattering Coefficients

Spectrally resolved reflectance measurements can measure the absorption and scattering coefficients. Light is incident on the target and is collected at different source-detector distances (SDD). Spatially resolved diffused reflectance has been shown to be

able to resolve the absorption and scattering coefficients in tissue simulating phantoms [22].

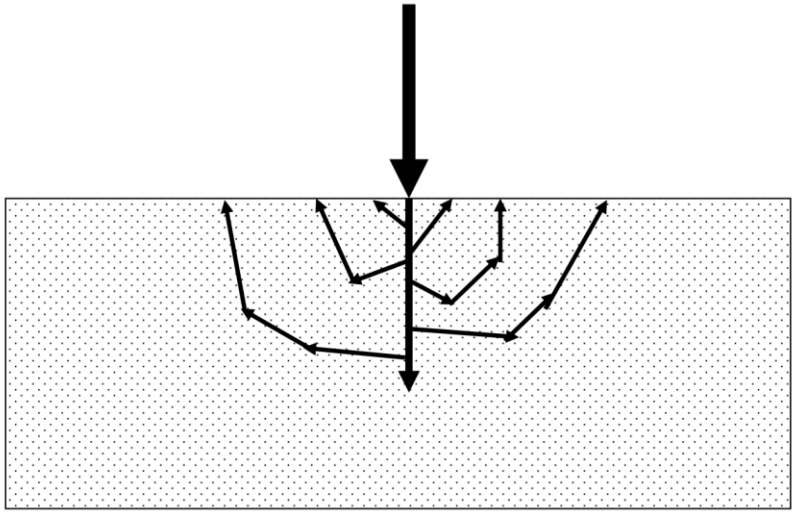

Figure 2-2. Spectrally resolved DR measures reflectance as a function of SDD in a turbid medium.

Another method of measuring optical properties is the use of an integrating sphere. An integrating sphere is a sphere coated with a highly scattering substance such that all points on the sphere are assumed to be irradiated equally. By using an integrating sphere with a reflectance standard, one can calculate the transmittance and reflectance of a test sample. It is possible to retrieve absorption and scattering coefficients using an integrating sphere [23].

Time-resolved reflectance measurements can also retrieve optical properties [24]. In the time-resolved method, a short pulse of light (few ps) is fired at the tissue and the reflectance intensity as a function of time is measured. The absorption coefficient can be estimated by the slope of the log plot of reflectance. The reduced scattering coefficient can also be estimated from the absorption coefficient and the highest probability arrival time [25].

2.2.2. Fluorescence Spectrum and Lifetimes

Fluorescence spectra are typically measured with a diffraction grating spectrometer.

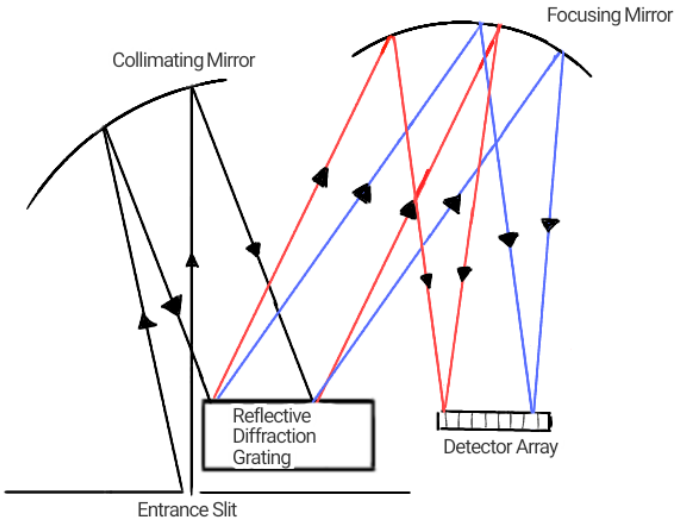

Figure 2-3. Schematic of a diffraction grating spectrometer

Other devices that provide spectral resolution are acousto-optic tunable filters (AOTF) and liquid crystal tunable filters (LCTF). AOTFs are bi-refringent crystals (typically Quartz or Tellurium dioxide) through which an acoustic wave is passed, resulting in a periodic change in refractive index. For a chosen acoustic frequency, only certain wavelengths meeting a momentum-matching condition will be diffracted, resulting in a bandpass filter with the diffracted wavelength varying with the acoustic frequency. LCTFs are based on a Lyot stage: a device consisting of 2 polarizers and a waveplate. A Lyot stage's transmission is a function of wavelength, and when multiple of them are placed in tandem, the transmission can be a narrow wavelength band. LCTFs vary the retardation in the waveplate by varying a voltage, resulting in a voltage-controlled tunable filter. LCTFs have lower spectral resolution, less out-of-band suppression and slower switching speed compared to AOTFs. However, LCTFs have a better spatial resolution [26,27].

Fluorescence lifetimes can be measured in several methods. One method is Time-Correlated Single-Photon Counting (TCSPC). The working principle of TCSPC is that the fluorescence decay profile corresponds to the probability of arrival times of photons. Thus, single-photon detectors are used to time the arrival of at most one photon after each excitation pulse, and then the arrival times are binned. If more than one photon is

received for one excitation pulse, the results will be skewed towards faster arrival times. An example TCSPC setup is shown in [28].

Another way of measuring fluorescence lifetime is by gated detection. Intensified charge-coupled devices (ICCD) are capable of being quickly (~100 ps) switched on/off. Thus, if an ICCD is switched on briefly after a laser excites a fluorophore, it would capture part of the fluorescence decay. If the ICCD's measurement window is delayed with respect to the first measurement window, the ratio of the 2 recorded intensities can be used to estimate the fluorescence lifetime [29]. Alternatively, the ICCD's gate can be delayed in small intervals (50 ps, for example), and the whole fluorescence decay convolved with the instrument response can be captured.

The time-resolved method used in this thesis is the time-sampling method. It utilizes a fast-response detector combined with a high sampling rate digitizer to sample the detector's output voltage. Microchannel plate photomultiplier tube (MCP-PMT) is a fast detector with a large number of capillaries several microns in diameter. Secondary electrons are emitted in the walls of the capillaries, and those replace the dynodes in a conventional PMT. Electron transit time in the capillaries is very short, allowing for small transit time spread, resulting in good temporal resolution. The fast response (few hundred ps) and high gain (voltage-dependent, can be $>10^4$) make them ideal for time-sampled fluorescence decay measurement.

Frequency Domain (FD) methods use a modulated light source and a modulated detector. In homodyne mode, the light source and detector are modulated at the same frequency, and their phase difference is changed to obtain a time-domain phase shift and demodulation, from which the lifetime can be calculated. In heterodyne mode, the light source and detector are modulated at slightly different frequencies, so that the resulting waveform will have a low frequency but retains the phase and modulation of the emitted waveform. An example of a FD-FLIM microscope is given in [30].

2.3. Algorithms and Processing

2.3.1. Absorption and Scattering coefficients

The method of calculating absorption and scattering coefficients as well as anisotropy will depend on the measurement method used. For spatially resolved DR, one method of retrieving the parameters is by creating a lookup table (LUT). The lookup table can be produced by measuring the reflectance of phantoms as a function of SDD. This creates a mapping from the reflectance domain to the absorption and scattering domain [31].

One of the limitations of this approach is that any uncertainty in the optical properties of the phantoms carries over to the lookup table. Additionally, any differences between the phantoms and actual targets will affect the accuracy of retrieved absorption and scattering coefficients. For example, the phantom might not reproduce the scattering anisotropy of tissue. Phantoms may use lipid emulsions or polystyrene microbeads as scattering material, and black India ink as a pure absorber.

LUTs can also be made by Monte Carlo simulations, using the transport equation with certain approximations and assumptions. Commonly, the input beam is approximated as a pencil beam, and the phase function is assumed to be a Henyey-Greenstein phase function. The value of the anisotropy coefficient is also usually approximated to reflect that of tissue. The inverse Monte-Carlo method is computationally expensive, so it cannot be used to analyze reflectance data in real-time.

Besides simulations and phantoms, a closed form solution of the diffusion approximation of the transport equation can give radial intensity as a function of distance from the source. The absorption and scattering can be calculated with non-linear fitting techniques. This method also has assumptions, such as that the medium is highly scattering, and the source is a pencil beam [32].

2.3.2. Fluorescence Lifetime

In its simplest form, retrieving the fluorescence lifetime equates to finding the mean arrival time of all photons, given by $\tau = \frac{\sum N_i t_i}{\sum N_i}$, Where N_i is the number of photons arriving at time t_i.

One method of finding this value is rapid lifetime determination (RLD), where the fluorescence decay is integrated over two regions of equal width, and the ratio of the integrals is used in equation **2.7**.

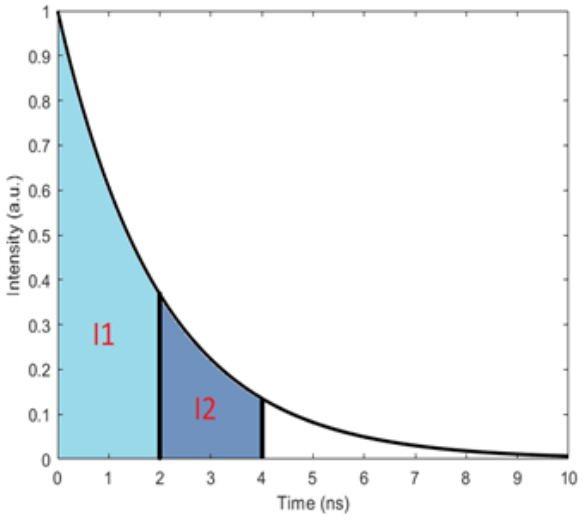

$$\tau = -\frac{\Delta t}{\ln\left(\frac{I_2}{I_1}\right)} \qquad \textbf{(2.7)}$$

Figure 2-4 Illustration of RLD

RLD is non iterative and only requires two collection gates, making it a very fast method for retrieving the lifetime. Its error is similar to the linear least-squares method, with low error under the condition $\Delta t > \tau$ [33].

Another method of finding the lifetime is the center of mass method (CMM). This method makes the approximation that the distance between the origin of the decay and its center of mass is equal to the lifetime. This approximation is only valid if the tail of the decay is not truncated ($T>7\tau$). Additionally, CMM requires many time bins (~1000) to calculate the center of mass with low uncertainty, as opposed to RLD which requires only two time bins. However, CMM keeps the benefit of speed and its implementation depending only on summation, which is suitable for programming onto an FPGA [34].

Another method of lifetime retrieval is linear least-squares fitting, where a straight line is fit to the logarithm of intensity values as a function of time, and the slope is used to calculate the lifetime.

$$\ln(I) = \frac{1}{\tau}t + C \quad \textbf{(2.8)}$$

All 3 methods mentioned above are only suitable for retrieving the average measure of a lifetime. However, sometimes it is required to resolve multiple fluorescence lifetime components and their relative contributions. More advanced methods exist for accomplishing this. The most common method is non-linear fitting, typically using the Levenberg-Marquardt algorithm (LM). The LM algorithm is a combination of Newton's method and gradient descent which minimizes an error function of multiple parameters. The LM algorithm needs a model of the decay to fit to. This may not be easy to produce if the target has an unknown number of fluorescent components. A bi-exponential model is typically used:

$$I = ae^{-\frac{t}{\tau_1}} + (1-a)e^{-\frac{t}{\tau_2}} \quad \textbf{(2.9)}$$

LM aims to minimize a cost function. Equation **2.10** shows an example of a cost function.

$$E = \frac{1}{N}\sum_{i=1}^{N}\left(d_i - F(x_i, \boldsymbol{w})\right)^2 \quad \textbf{(2.10)}$$

d_i is the i^{th} point in the data array (i.e. measured intensity), x_i is the independent variable (i.e. time), F is the model function and $\boldsymbol{w}$ is a vector of parameters to be optimized (i.e. lifetimes and weights). To minimize error quickly and robustly, in each iteration, the weight vector is adjusted using equation **2.11**.

$$\Delta \boldsymbol{w} = [\boldsymbol{H} + \lambda \boldsymbol{I}]^{-1}\boldsymbol{g} \quad \textbf{(2.11)}$$

Where $\boldsymbol{g}$ is the error gradient vector and $\boldsymbol{H}$ is its Hessian. λ is a regularization parameter, which changes the LM algorithm to Newton's method if set to 0. The iterative nature of this algorithm makes it slow compared to a non-iterative approach.

Another method of retrieving multiple lifetime components and their contributions is the phasor analysis approach [35]. This method was developed to analyze FD-FLIM data. However, it can also be used for time-domain decays [36]. The phasor approach uses the properties of the Fourier transform of an exponential decay function. *G* and *S* are defined below.

$$G(\omega) = \frac{\int_0^\infty I(t)\cos(\omega t)dt}{\int_0^\infty I(t)\,dt} \quad \textbf{(2.12)}$$

$$S(\omega) = \frac{\int_0^\infty I(t)\sin(\omega t)dt}{\int_0^\infty I(t)dt} \quad \textbf{(2.13)}$$

For a single exponential decay, $I(t) = e^{-\frac{t}{\tau}}$, *G* and *S* evaluate to:

$$G(\omega) = \frac{1}{\tau^2\omega^2+1} \quad \textbf{(2.14)}$$

$$S(\omega) = \frac{\omega\tau}{\tau^2\omega^2+1} \quad \textbf{(2.15)}$$

By equation **2.16**, (*G*, *S*) form a semicircle, with radius 0.5, centered at *(0.5, 0)*. Additionally, there exists a simple relationship between *G, S, ω,* and τ.

$$(G - 0.5)^2 + S^2 = 0.5^2 \quad \textbf{(2.16)}$$

$$\tau = \frac{1}{\omega}\frac{S}{G} \quad \textbf{(2.17)}$$

For a multi-exponential decay, $I(t) = \sum f_i e^{-t/\tau_i}$

$$G(\omega) = \sum \frac{f_i}{\tau_i^2 \omega^2 + 1} = \sum f_i G_i \quad \textbf{(2.18)}$$

$$S(\omega) = \sum \frac{\omega \tau_i f_i}{\tau_i^2 \omega^2 + 1} = \sum f_i S_i \quad \textbf{(2.19)}$$

By equations **2.18** and **2.19**, phasors for a multi-exponential decay are the linearly weighted sum of each individual component's phasor. This property allows extractions of fractional components easily through a straight-line fit assuming there are 2 components.

The advantage of the phasor method lies in its speed, since no iterative solving is required. It is also versatile in the sense that it can calculate fractional components of fluorescence even for mixtures of fluorophores each with multi-exponential decays. However, its drawback is that unlike non-linear fitting, a single decay is not enough to extract both the lifetimes and their fractional components.

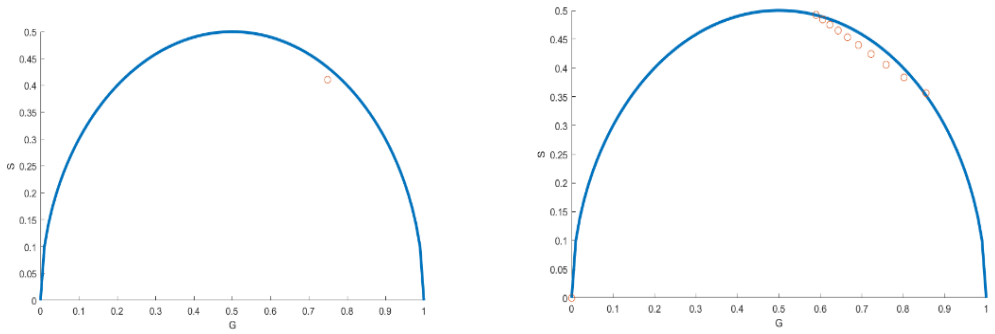

Figure 2-5. **(left)** Illustration of expected phasor point from a multi-exponential decay. **(right)** Expected phasor points from bi-exponential decays of varying weights

Both the LM fitting and phasor approach would give skewed lifetimes when the fluorescence lifetime is within two orders of magnitude of the instrument response function (IRF) width. That is because the measured decays are the result of convolution of the intrinsic decay functions, *h(t)*, with the IRF, $x(t)$. There are methods for deconvolving the intrinsic decay function from the instrument response. For example, in the LM approach, a fit to the convolution of the biexponential with the IRF is performed. The cost function becomes:

$$E = \frac{1}{N}\sum_t [\, y(t) - h(t) * x(t) \,]^2 \quad \textbf{(2.20)}$$

In the phasor domain, the instrument response can be compensated for using the instrument response's Fourier transform, or using a calibration sample with a known lifetime [37].

Another method of deconvolution is to represent the decays in an orthogonal basis. An example of this is Laguerre deconvolution, which approximates the decays as a finite sum of Laguerre functions [38].
The Laguerre functions form an orthonormal and complete basis for the space of square-integrable functions, so that an arbitrary function *f(t)* can be approximated to arbitrarily small error in that basis. In this method, the intrinsic fluorescence response is approximated as a sum of Laguerre functions of order up to *L*, with coefficients c_j. The Laguerre functions are defined up to a scale parameter α below [39].

$$b_j^{\alpha} = \sqrt{1-\alpha}\, e^{-\frac{(1-\alpha)t}{2}} L_j(\,(1-\alpha)t\,) \quad \textbf{(2.21)}$$

$$h(n) = T \sum_{j=0}^{L-1} c_j b_j^{\alpha}(n) \quad \textbf{(2.22)}$$

The measured signal can then be expressed as:

$$y(n) = \sum_{j=0}^{L-1} c_j v_j(n) \quad \textbf{(2.23)}$$

Where v_j is the convolution of the IRF with the Laguerre function of order *j*. The coefficients c_j can then be found by solving the linear minimization problem:

$$\underset{\boldsymbol{c}}{\operatorname{argmin}} |CV - Y| \quad \textbf{(2.24)}$$

The Laguerre deconvolution, if successful, returns the intrinsic fluorescence as a function of time. It is also fast, as the deconvolution problem reduces to a linear minimization problem with only a few parameters. However, it does not return a fluorescence lifetime or fractional components. Thus, after deconvolution, one of the methods mentioned above may need to be used to retrieve a lifetime, or the Laguerre coefficients can be treated as the parameters to create contrast between different samples of different fluorescent decays. For comparing results with previous and future works, it is desirable to have a fluorescence lifetime since it is the most intuitive and commonly used parameter in fluorescence decay dynamics.

Chapter 3

DR-TRF Instrument Design, Assembly, and Characterization

3.1. Design Requirements

The intent for the DR-TRF instrument is to be able to acquire data which may be relevant to optical biopsies. These quantities include the absorption and scattering coefficients, fluorescence peak wavelengths, lifetimes and relative contribution of individual fluorophores in the target. The acquisition properties necessary to achieve this goal are outlined below.

Excitation source: The excitation source should be a short pulse (sub-ns) to allow resolution of fluorescence lifetimes which are in the few-ns timescale [40].The excitation wavelengths should fall within the absorption spectra of endogenous fluorophores of interest. NAD(P)H, FAD, Collagen and elastin can be excited by 355 nm light [41]. The source's energy per pulse should be as large as possible without damaging the target [42]. The repetition rate should be high enough to collect sufficient signal in a short time frame to resolve fluorescence lifetimes. More than one excitation source may be used to excite different fluorophores separately [43].

Time-resolved detection: The instrument's temporal response should be fast enough to be able to resolve fluorophores with lifetimes in the range of 100ps to 10 ns. The detector needs high quantum efficiency and sensitivity over the wavelength range of interest. Since signal intensity may vary significantly in different targets and at different detection wavelengths, adjustable gain or large dynamic range are required of the detector and digitizer. For time-sampled fluorescence lifetime measurement, the instrument needs a digitizer with high bandwidth and sampling rate. Additionally, it is very desirable to be able to separate the fluorescence decays into bands of wavelengths, either through a series of dichroic mirrors (multispectral) or a tunable filter (hyperspectral).

Reflectance measurements: The requirement is a light source with a large wavelength range and high power, since the light retrieved from diffuse reflectance is only a fraction of the light incident on the tissue. The wavelength range must include the fluorescence emission of collagens, FAD and NAD(P)H for performing corrections to fluorescence spectra and calculating intrinsic fluorescence. Additionally, the wavelength

range must extend enough into the red or infrared range for detecting changes in lipid and water content. For spatially resolved DR, another requirement is to have collection fibers at fixed and known distances from the source fiber. Additionally, the system must have a way of normalizing the DR data. This can be achieved by using a reflectance standard before measuring the target. Alternatively, DR data can be normalized by splitting the source light using partial reflecting mirrors and normalizing against the source light at the time of measurement. The detector should have good wavelength resolution (~1nm) and variable integration times since the signal may vary significantly depending on the absorbers present in the target.

Overall performance: One of the overall requirements of the system is speed. Since an optical biopsy system is intended to be deployed in a surgery setting, it is critical that the acquisition does not extend the duration of the surgery significantly. An acquisition time on the order of 1 second per point is appropriate for this purpose. Another requirement is a spatial resolution around 1 mm, since tumor margin resection differences of a few millimeters have been shown to affect patient outcome [45]. To retrieve intrinsic fluorescence spectra, DR and TRF sub-systems should be integrated so that they probe the same volume.
The system should have the processing power, algorithms, and calibrations necessary to convert the DR-TRF data to **a)** fluorescence lifetimes and relative contributions, **b)** absorption and scattering coefficients, **c)** Intrinsic fluorescence spectra. Lastly, in order to be used for optical biopsy, the instrument should have sufficient data from positive and negative patient cases.

3.2. Design Schematics and Components

System A is a DR-TRF instrument previously used to investigate optical biopsy for brain tumors [2]. It meets the requirements laid out above and is used in this thesis for the acquisition of the data for chapters 4 and 5. The design of a newer version of the DR-TRF instrument (system B) is presented and the performance of the two systems is compared. The schematic of system B is shown in figure 3-1.

The fluorescence excitation source is a 355 nm, 300ps FWHM pulsed Nd:YAG laser (PNV-M02510-130, Teem Photonics, Meylan, France). It is reflected by a UV mirror (BB1-E01, Thorlabs, >99% reflection 350-400 nm), which controls its angle of incidence on the dichroic mirror. Before reflecting on the dichroic mirror, the laser's intensity is reduced by an ND filter (NDL-10S-4, Thorlabs, variable OD: 0.1 - 4.0). The laser is then partially reflected by the dichroic mirror (FF01-380/LP-25, Semrock, 56% reflection of 355 nm at 45° incidence, >94% transmission from 370nm to 550 nm). The laser is coupled into the fiber (Optran WF, Ceramoptec, NA = 0.12, 400 μm) using a plano-convex lens (LA4130, Thorlabs, f=40.1 mm, Ø = ½). The fluorescence light is partially collimated by the plano-convex lens (L1), transmitted through the dichroic mirror, and then diffracted by the AOTF (TEAF5-0.36-0.52-S-MSD, Brimrose, Baltimore, MD). The diffracted e- and o- beams are focused onto the MCP-PMT (R5916-50, Hamamatsu Photonics, Japan) by concave mirrors (CM254-100-E02, Thorlabs, f=100mm, Ø

=25.4mm, >95% reflectance 380-550 nm). Scattered laser light is attenuated by a UV filter (BLP01-355R-25, Semrock, OD > 6 at 355 nm).

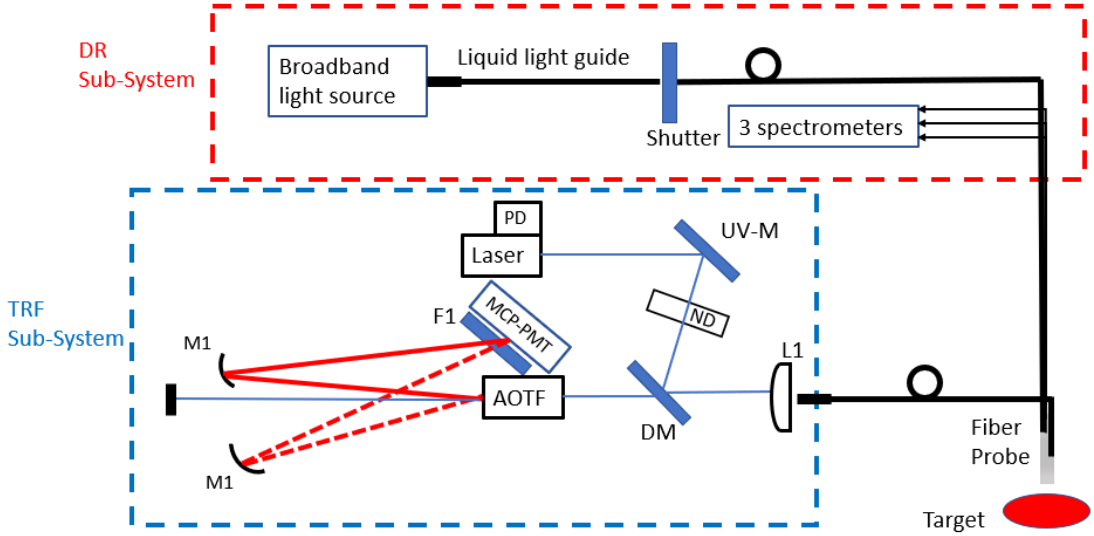

Figure 3-1. Schematic of System B. PD: photodiode, UV-M: UV mirror, ND: neutral density filter, DM: dichroic mirror, L1: plano-convex lens, AOTF: acousto-optic tunable filter, M1: concave mirror, F1: UV filter, MCP-PMT: Microchannel plate photomultiplier tube.

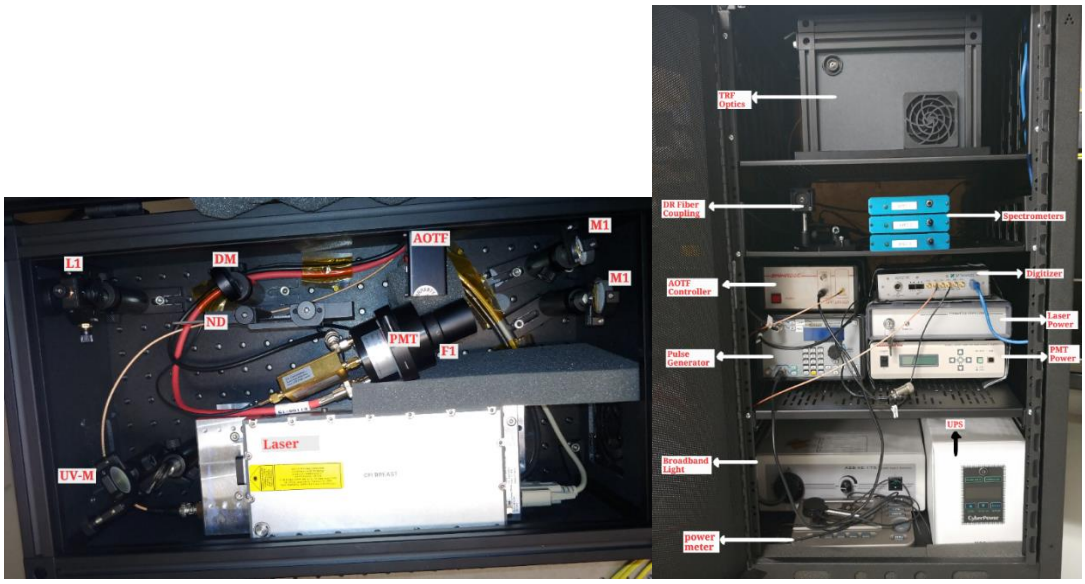

Figure 3-2. **(left)** Overhead view of the TRF optics. **(right)** Front view of cart housing the DR-TRF system, showing the electronic components.

Integrated with the TRF sub-system is the DR sub-system. A Xenon lamp emits the broadband incident light (ASB-XE-175BF, Spectral Products, NM, USA), and a liquid light guide (AF5000-50001111-VIS10S, Spectral Products) carries the light to a custom-built shutter which only opens during DR measurements. The light is coupled directly to the DR delivery fiber (Ceramoptec NA=0.22, 200 μm). The 3 collection DR fibers deliver the diffuse reflected light to 3 spectrometers (BW-UVIS 600g/mm 50μm slit, StellarNet, Tampa, FL).

Electronics of interest that were not mentioned above are the digitizer (ADQ7DC, 14 bit, 10 GS/s, 2.5 GHz bandwidth, SP Devices, Sweden), amplifier after PMT (C5594-12, Hamamatsu Photonics, Japan) and delay generator (QC9522, Quantum Composers, MT, USA). Additionally, a laptop computer interfaces with the pulse generator and saves the spectrometer's and digitizer's readouts. The integration of DR and TRF sub-systems is accomplished with a bifurcated fiber bundle. The face of the probe and its schematic are shown in figure 3-3.

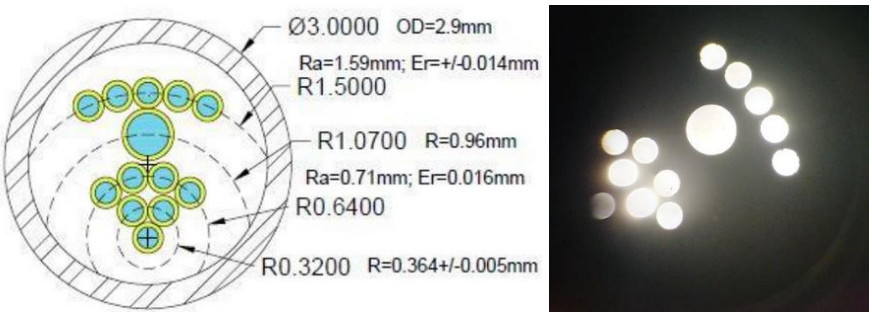

Figure 3-3. **(left)** Schematic of fiber bundle. The bottom-most fiber is the DR source, and the equidistant sets of fibers are the DR collection fibers. DR fibers are all 200 microns in diameter. The 400-micron diameter fiber is the TRF excitation and collection fiber. **(right)** image of probe face when all fibers are illuminated with a desk lamp.

The probe design was based on maximizing collection efficiency of DR and TRF fibers [47] and the ability of DR fibers to extract absorbance and scattering coefficients from the reflectance data at each source-detector distance [48]. Another consideration in the design of the fiber probe is that the epoxy holding the fibers together should not fluoresce significantly under 355 nm illumination, otherwise it would add a background fluorescence.

3.3. DR-TRF Acquisition Procedure

The acquisition is controlled by a custom C++ software, whose interface and bock diagram are shown in figure 3-4.

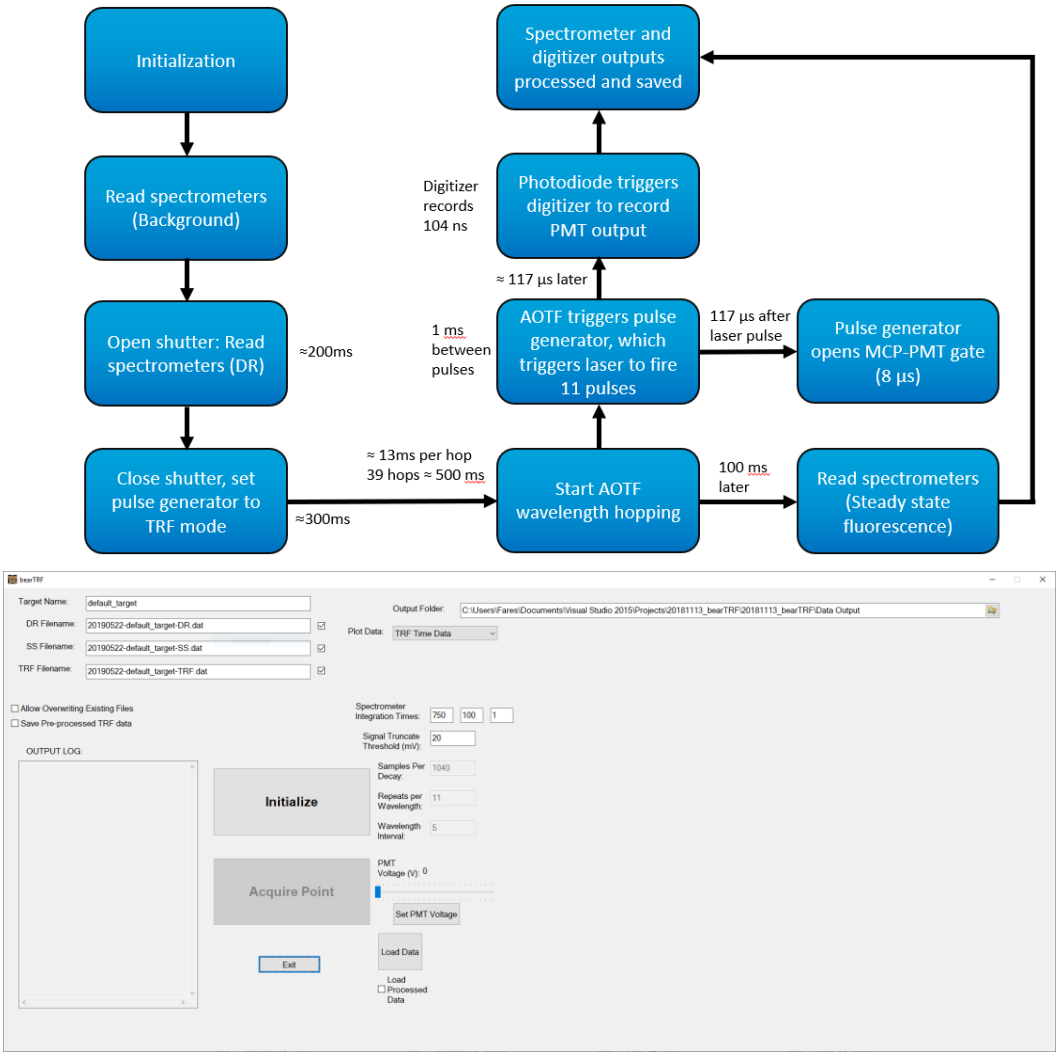

Figure 3-4. **(top)** Block diagram of acquisition procedure of system B. **(Bottom)** Screenshot of GUI.

In the initialization step, the digitizer is initialized to be triggered by the photodiode and to record 39*11 (=429) records, of 1040 samples each. The AOTF controller is initialized to hop from wavelength 380 nm to 570 nm, at intervals of 5 nm (=39 wavelengths). At every wavelength hop, the AOTF controller sends a synchronization pulse that triggers the pulse generator. The spectrometers are initialized with the selected integration times. Lastly, the AOTF controller, PMT power supply, and digitizer are queried to find if their initialization was successful.

The GUI allows plotting the acquired data in real time, which provides a quick visual verification of the data. The format of the DR data is 4 columns of comma separated numbers (saved by default as ascii text). The first column is wavelength, while the other 3 columns are intensity in arbitrary units, after background subtraction. The format of the raw TRF data is 429 columns, each with 1040 numbers. Each column contains a single decay, and every 11 consecutive columns represent all decays at a single wavelength.

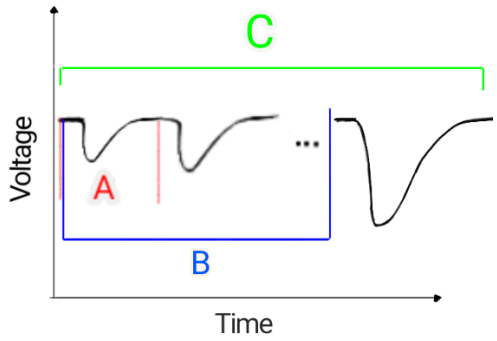

Figure 3-5. TRF data format. A = 1040 samples per decay. The voltage has a positive DC offset, and the PMT signal has a negative polarity. B = 11 repeats per wavelength, which are averaged to increase signal-to-noise ratio. Changing B equates to changing integration time of the TRF system. C = 39 wavelengths, starting at 380 and ending at 570 nm.

3.4. Design Choices and Calibration

The digitizer was chosen for its high sampling rate, bandwidth and bit depth. Chapter 4 includes a simulation showing the effects of these parameters on uncertainty in retrieved decays. MCP-PMT was chosen for its fast response time (180 ps rise time), low transient time spread (90 ps), and high gain which can be controlled over a large range ($>10^2$ - 10^5). An AOTF was chosen for its high spectral resolution (0.8 – 4 nm), fast switching speed (ns timescale), and wavelength range covering most of the visible spectrum and extending into the UV region.

The calculations justifying the choice of the lens L1 are presented. Then, two calibrations for the AOTF are explained: one for AOTF driver's power, and the other for the angle relative to the incident beam. Lastly, calibration of the PMT's spectral response is performed using dyes and a spectrometer.

3.4.1. Lenses and Mirrors

The lens L1 must meet the following objectives:

- Couple laser light into a fiber with 0.12 numerical aperture (NA).
- Collimate fluorescence light from the fiber to within the AOTF's acceptance angle (4 degrees).
- Make spot size of fluorescence light smaller than AOTF's window (5 mm).

- Show negligible fluorescence due to 355 nm light.

The chosen lens is a UV fused silica lens of focal length 40.1 mm and a diameter of 12.7 mm. This equates to a numerical aperture (NA) of 0.158. This is greater than the optical fiber's NA of 0.12, so the forward coupling is not ideal since the convergence angle into the fiber is greater than its acceptance angle. However, this design allows both forward coupling and back coupling with a single lens, reducing signal loss at interfaces. The requirements for forward coupling are a numerical aperture close to that of the fiber, and that the fiber is placed close enough to the focal point such that the spot size is not greater than the core diameter (400 microns). The incoming light is assumed to be collimated (divergence angle < 4mrad) and has a beam diameter of roughly 1 mm. The schematic for forward coupling is shown below.

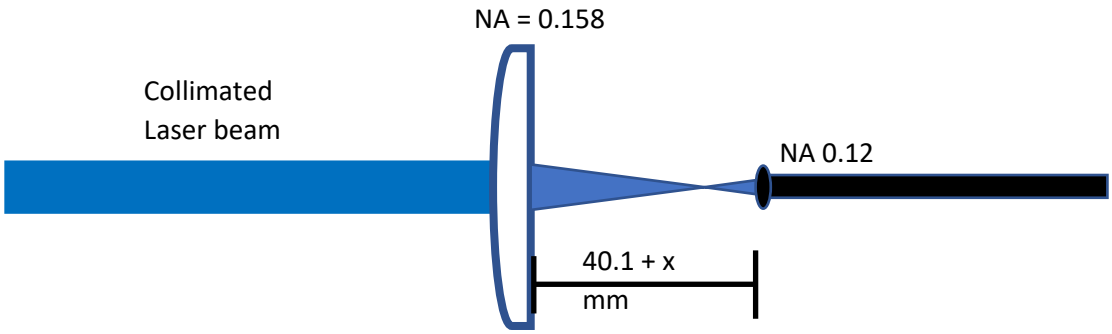

Figure 3-6. Ray diagram of forward coupling of laser into the TRF fiber.

Letting *x* be the offset of the fiber from the focal point of the lens, calculate a value of *x* such that the spot size at the fiber face is less than the fiber core diameter:

$$0.158\,x \approx 0.2\,mm \rightarrow x \approx 1.3\,mm$$

The requirements for back coupling are that the light is collimated to within 4 degrees, and that spot size is smaller than 5 mm at the entrance and exit of the AOTF. If *x* is 1.3 mm and the AOTF is 300 mm away from the lens, these conditions are met. Using the lens equation to find distance from the lens to the point where fluorescence spot is focused:

$$\frac{1}{a}+\frac{1}{b}=\frac{1}{f} \rightarrow \frac{1}{41.4}+\frac{1}{focal\ distance}=\frac{1}{40.1} \rightarrow focal\ distance = 1277\,mm$$

Thus, the convergence half-angle is: (Approximating fiber as a point source)

$$\frac{9.93}{2 * 1277} rad = 4\,mrad = 0.22\,degrees$$

The spot size 300 mm away from the lens is:

$$spot\ size = 0.004 * 2 * 300 = 2.4\,mm$$

2.4 mm is small enough to enter the AOTF's aperture. Thus, this design meets both the angle and spot size requirements of the AOTF using a single lens, with the trade-off of sub-optimal forward coupling.

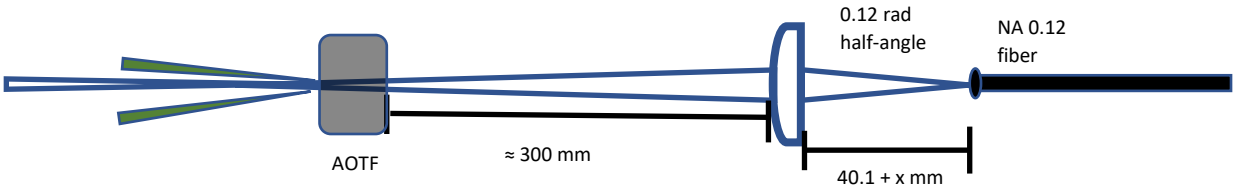

Figure 3-7. Ray diagram of back-coupling of fluorescence light into AOTF and ultimately into the detector window.

In reality, when aligning the optics, the 1.3 mm offset from the focal point was not measured, but the fiber was moved away from the lens until the collected light's focal point is after the AOTF. Thus, the angles and distances calculated above are only approximations and will differ if the lens L1 is moved along the optical axis. With this setup, a coupling efficiency of 60% was measured with a power meter (J-10MT-10KHZ, Coherent, CA, USA). For an input power to the fiber of 5.5 mW, an output power of 3.3 mW was recorded.

3.4.2. AOTF

The following 2 calibrations were needed for the AOTF:

1) Spectral differences between the o- and e- beams are minimized. This is done by changing the angle of the AOTF relative to the incoming fluorescence beam.

To perform this calibration, a white light source was shone through the probe end of the fiber, and one spectrometer's aperture (BW-UVIS, Stellarnet) was aligned with the o- and e- beams of the AOTF. The AOTF was then rotated in its post, and the difference between the o- and e- beams recorded. The angle was calibrated such that the spectral difference between the o- and e- beams at the wavelength of 510 nm is minimized. However, at wavelengths far from 510 nm, the differences between the o- and e- beams become apparent, as in figure 3-8.

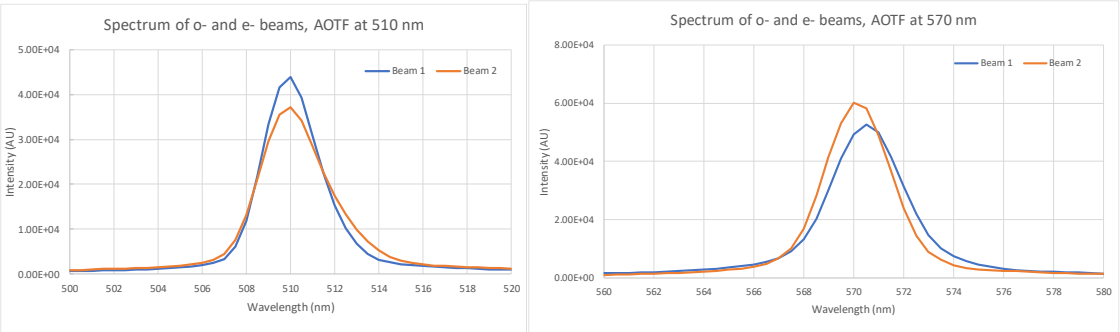

Figure 3-8. Spectrum of o- and e- beams exiting the AOTF when the selected wavelength is 510/570 nm.

2) Radio frequency (RF) power into the AOTF is controlled to maximize diffraction efficiency

One of the parameters in controlling the AOTF is the RF power delivered by the AOTF driver. As shown in figure 3-9, low power causes a low diffraction efficiency and a power too high causes spectral broadening. A lookup table is created giving the highest power without significant spectral broadening at each wavelength.

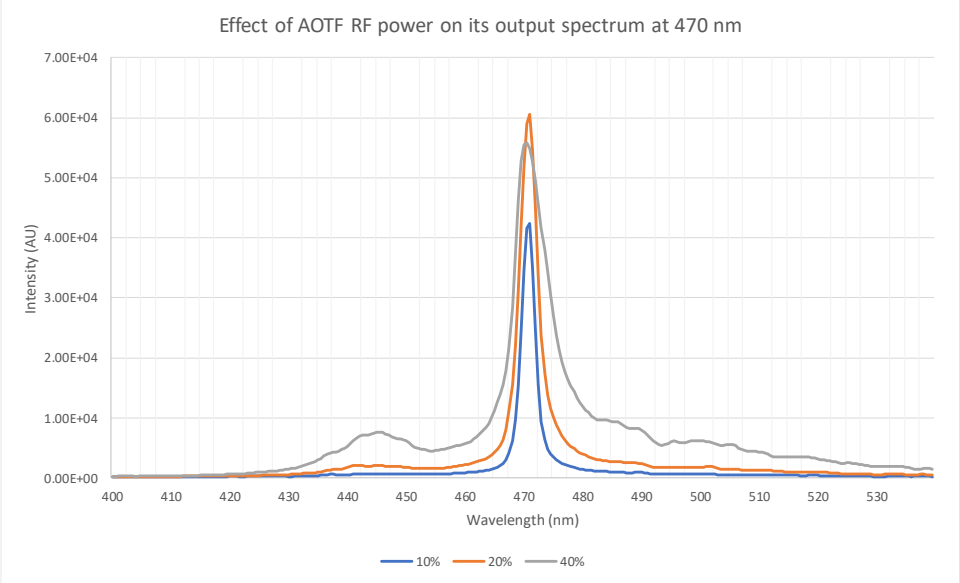

Figure 3-9. Output of AOTF at different RF powers. When power exceeds a certain threshold, the output spectrum broadens.

3.4.3. PMT Spectral Calibration

A sensitivity calibration for the MCP-PMT was created such that the integral of the PMT's readout at each wavelength produces an identical spectrum as the spectrometer. To this end, spectra of dyes were measured using both the MCP-PMT (TRF system) as well as the spectrometer, and the ratio of the measurements acts as a sensitivity

calibration. Three dyes are prepared: The first is coumarin-6 (Sigma Aldrich 442631-1G). The second is 9-cyanoanthracene (Sigma Aldrich 152765-5G). The third is Fluorescein (Sigma Aldrich F2456-2.5G). All the dyes were dissolved in anhydrous ethanol at a concentration of 10 μM. First, the following masses and volumes were mixed to create 1 mM solutions. Masses were measured by a lab scale (1 mg precision) and volumes by a beaker (5% uncertainty):

$$m_{C6} = 16 \pm 1\ mg; V_{C6} = 45.7 \pm 2\ mL$$

$$m_{9CA} = 8 \pm 1\ mg; V_{9CA} = 39.4 \pm 2\ mL$$

$$m_{FL} = 22 \pm 1\ mg; V_{FL} = 66.2 \pm 3\ mL$$

Next, 50 μL from each solution was pipetted into 5 mL of anhydrous ethanol to create 10μM solutions. Steady state and TRF measurements were taken on these samples. The sensitivity calibration was calculated as follows:

$$S(\lambda) = \frac{I_{PMT}}{I_{spectrometer}}$$

$$I_{PMT} = \int y(t)\, dt$$

One of the difficulties of this calibration is that it requires a fluorophore with an emission in the entire wavelength range from 380 to 570 nm. To overcome this problem, *S(λ)* was obtained as above using C6 for the wavelength range of 515 to 570 nm and 9CA was used to find *S(λ)* in the range of 405 nm to 510 nm. The sensitivity as a function of wavelength was normalized in both cases to equal "1" at 525 nm, a wavelength where both 9CA and C6 fluoresce. With this normalization, the sensitivity for the wavelength range 405 nm to 570 nm is shown in figure 3-10. The range 380 nm to 400 nm was not calibrated because the dyes did not have sufficient emission in that range. Another difficulty with this calibration is that the low dye concentrations of 10 μM leads to low signal-to-noise ratio in the spectrometer measurements, which translates to high uncertainty in the sensitivity calibration.

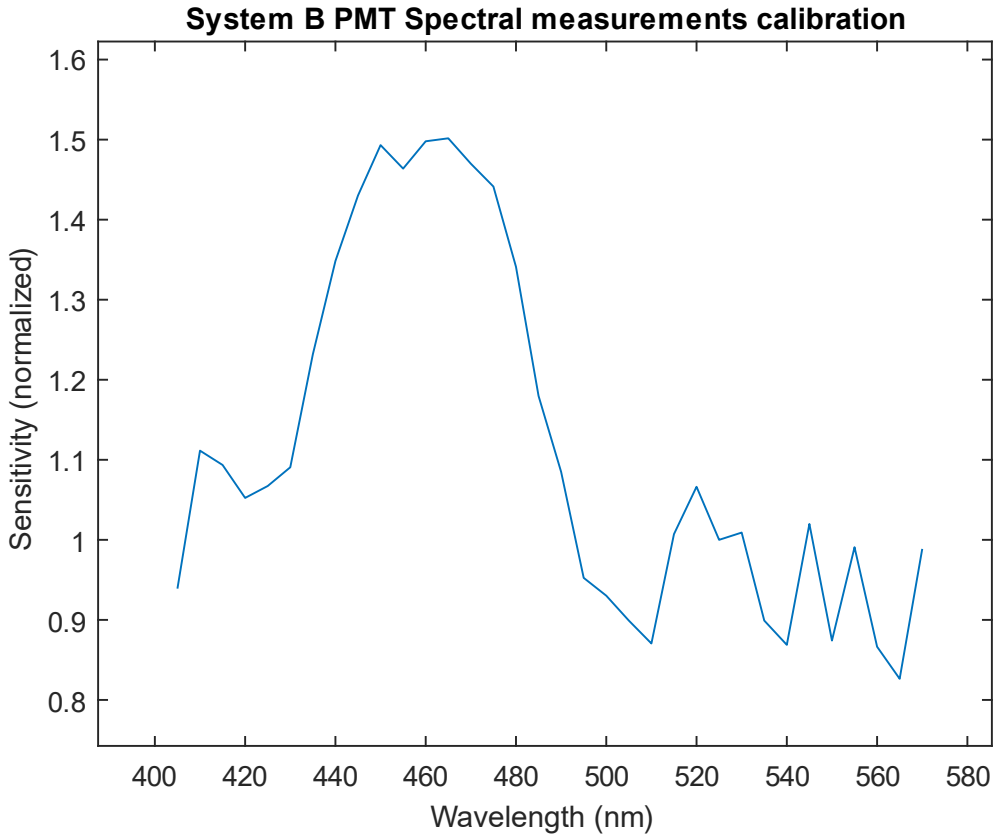

Figure 3-10. Sensitivity of PMT spectral measurements, calibrated by the ratio of PMT intensity to spectrometer intensity as a function of wavelength

3.5. System Validation

The TRF collection efficiency was validated by comparing it to that of system A. Additionally, the time resolution was tested by measuring the fluorescence lifetimes of standard dyes and comparing values to literature. To estimate the collection efficiency of system A, the laser power was measured as 2.0 mW with system A's power meter (3-sigma, Coherent). Next, the probe was placed perpendicular to and lightly touching a business card, and a hyperspectral TRF measurement was taken with a PMT voltage of 1500V. Nine measurements were taken, 3 at each region in the business card shown below.

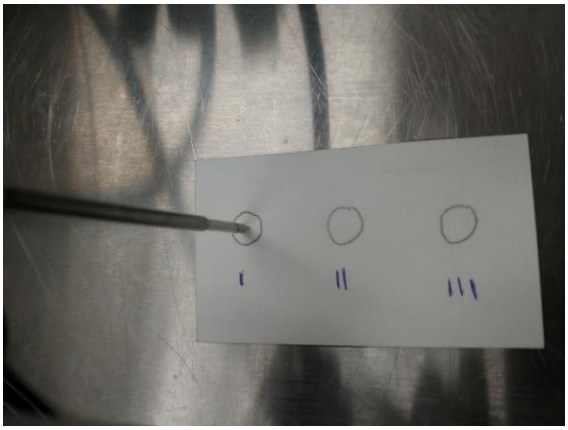

Figure 3-11. Business card used as a fluorescent target for comparing collection efficiency of systems A and B.

To measure system B's collection efficiency, the same business card was used and the laser power and PMT voltage were also 2.0 mW and 1500 V respectively. The laser power was measured with system B's power meter (J-10MT-10KHZ, Coherent).

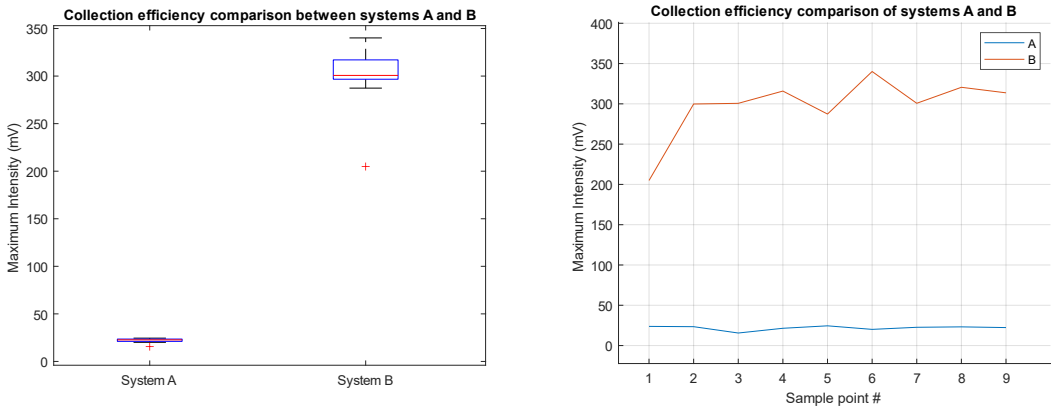

Figure 3-12. **(left)** Box plot of measured peak voltage with a paper target in systems A and B under similar conditions. **(right)** Measured maximal intensity values at each point.

Figure 3-12 shows that System B records a significantly higher maximum intensity compared with system A. The maximal intensities recorded by systems A and B are 22±3 and 298±38 mV respectively. Peirce's criterion is used to determine if the outlier in System B's measurement should be discarded:

$$R\sigma = | x_{outlier} - \mu |$$

For 9 observations, Peirce's criterion has an R-value of 1.824, leading to a maximum allowed deviation of 69 mV. This is less than the deviation of the outlier, 93 mV. Thus, the outlier should be discarded. This changes the mean intensity measured by system B to 310 mV. Possible causes for the outlier include measuring a photobleached point on the target or a separation between the probe and target in the outlier measurement.

To verify the temporal resolution and ability to capture low fluorescence signals, hyperspectral TRF measurements were then carried out with system B on the 10 μM dyes described in section **3.4.3**. The instrument response was obtained from Coumarin-6, by assuming that its lifetime is 2.5 ns. Coumarin-6 is a widely used fluorescent dye, and multiple labs have measured its fluorescence lifetime in ethanol to be between 2.4 and 2.6 ns over a large range of concentrations [46].

Using an iterative convolution with a single exponential model, the following fluorescence lifetimes as a function of wavelength were obtained.

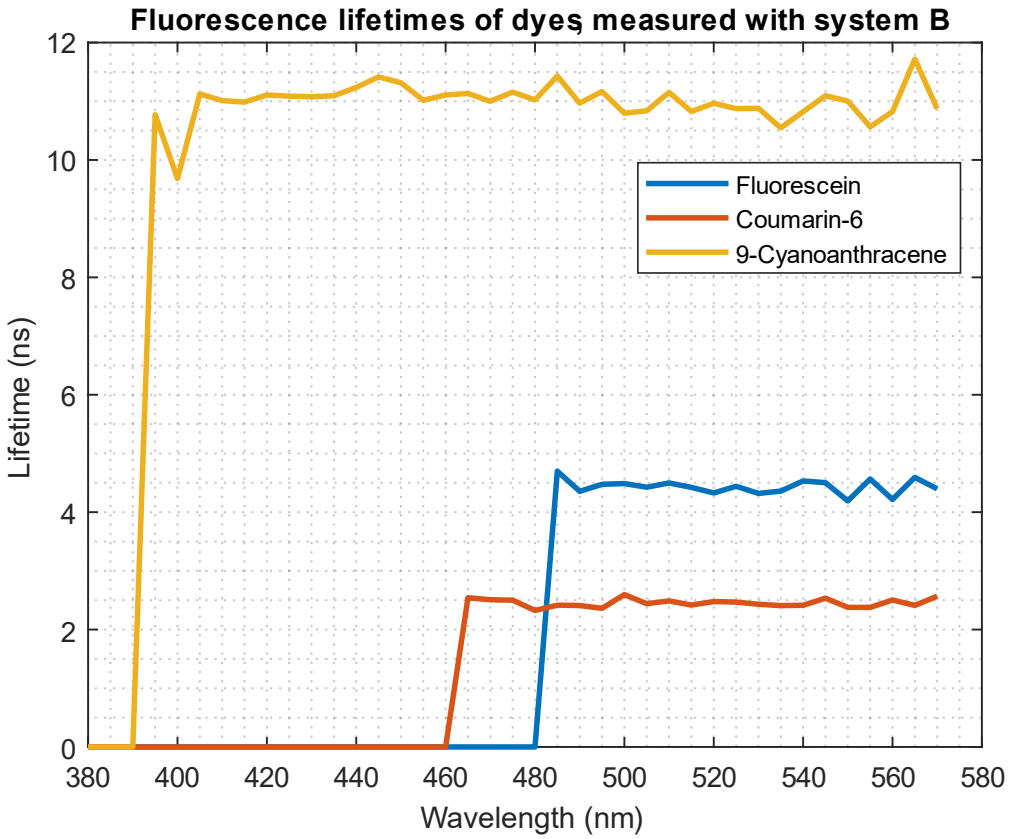

Figure 3-13. Retrieved hyperspectral fluorescence lifetimes from 3 dyes, measuring using system B.

In figure 3-13, the lifetimes are shown as 0 where the fluorescence intensity is below a threshold of 40 mV. The fluorescence lifetime for a single fluorophore is independent of the intensity, and so is constant across emission wavelength range. The standard deviation is on the order of a few hundred ps, which meets the time resolution requirement. The measured lifetimes agree with expected lifetimes from literature, which verifies that there are no large systematic errors apparent in the lifetime measurements of this system.

The broadband light source's spectrum was measured. It meets the requirement of covering the visible spectrum. However, the DR system's ability to resolve absorption and scattering coefficients was not investigated.

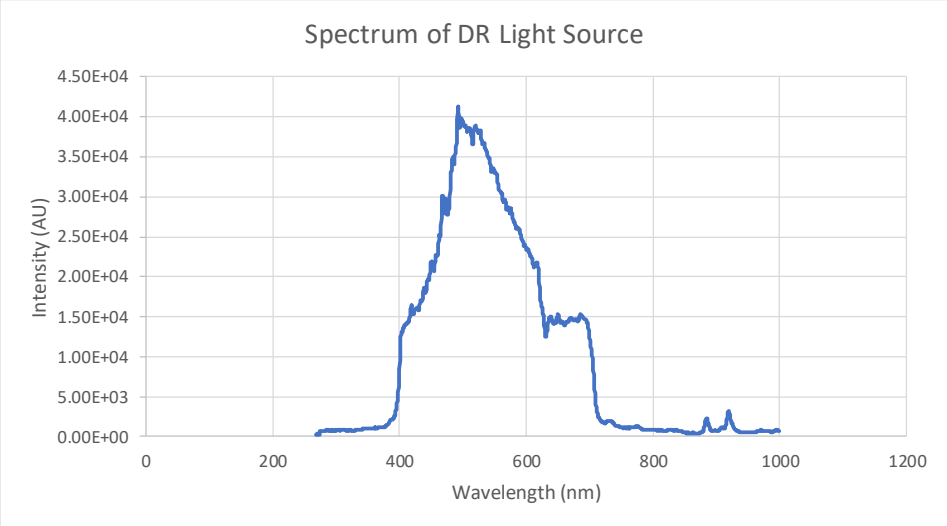

Figure 3-14. Spectrum of DR light source

The most significant difference between system A and B is the increase in the sampling rate from 3.6 Giga samples per second (GSPS) to 10 GSPS. This allows resolution of shorter lifetimes and decreases uncertainty for identical noise levels. Another difference is the optical coupling: System A uses an f=25.4 mm, Ø = 1″ lens, while system B uses an f=40.1 mm, Ø = ½″ lens. This leads to a smaller spot size at the AOTF entrance slit, and a converging beam entering the AOTF as opposed to a diverging beam. Figure 3-12 suggests that the collection efficiency is improved. The AOTF's accessible wavelength ranges are slightly different, with system A going to 550 nm, while system B goes up to 570 nm. A major improvement is the automation of the DR-TRF acquisition process and a user interface with control over PMT voltage as well as plotting features.

Chapter 4

Deconvolution and Fluorescence Lifetime Analysis

In order to train a classification model for optical biopsy, the data must be transformed into a few parameters that explain the observed data. For fluorescence decays, the parameters typically used are the fluorescence lifetimes and relative amplitudes. Many algorithms exist for this purpose, such as rapid lifetime determination [33], center of mass method [34] and global multiexponential fitting [50].

One of the difficulties of using these methods for endogenous fluorophores in biological tissue is choosing a model that describes the decays. One proposed method of tackling this challenge is a model-free fit in an orthonormal basis for the space of functions over the interval 0 to $+\infty$. The use of Laguerre functions as such a basis has been explored previously for this application [38]. Laguerre deconvolution is a model-free method for retrieving the intrinsic fluorescence, $h(t)$, given the measured fluorescence decay, $y(t)$, and the instrument response function (IRF), $x(t)$. However, Laguerre deconvolution faces the following difficulties:

1) It is only an approximation of the decay. It may lose valuable information if too few orders are used
2) It may fit to noise if the order used is too high
3) IRF needs to be known with relatively high certainty
4) Alignment of IRF with $y(t)$ can greatly affect results, introducing systematic errors
5) One of the inputs to the algorithms is a time-scale parameter, α, which can lead to poor fits if chosen incorrectly

Another challenge in analyzing TRF data is separating the fluorescence into components corresponding to different fluorophores and finding their relative contributions. This retrieves more information than calculating the average lifetime of a decay. A model-free method of doing this is using phasor analysis, where each fluorophore is assigned a unique coordinate in phasor space.

In this chapter, a simulation is performed to find the expected error when using Laguerre deconvolution under various conditions. The goal of the simulation is to give a guideline on what signal-to-noise ratio, sampling speed and instrument response time are necessary. Laguerre deconvolution is then combined with phasor analysis to show that the

two methods when used together can unmix the lifetimes and relative contribution of a mixture of 2 fluorophores. Dyes are used to demonstrate this capability.

4.1. Laguerre Deconvolution Simulation

The first step in the simulation is the creation of intrinsic decays which represent the 'true' solution. For a given lifetime, τ, discrete decays, *h(t)*, are created with time steps of 10 ps by equation **4.1**, starting from *t=0* until $t = 8\tau$. They are convolved with a Gaussian distribution with a FWHM of 500 ps, *x(t)*, which is an estimate of the IRF expected in the instrument described previously. Noise, *σ*, is then added to the 'measured' decay, *y(t)*, as in equation **4.2**. *σ* is taken to be normally distributed noise with a mean of 0 and a standard deviation given by equation **4.3**, where SNR is an input in the simulation.

$$h(t) = e^{-\frac{t}{\tau}} \quad \textbf{(4.1)}$$

$$y(t) = h(t) * x(t) + \sigma \quad \textbf{(4.2)}$$

$$std(\sigma) = \frac{max(y)}{SNR} \quad \textbf{(4.3)}$$

Next, *y(t)* is sampled according to the input sampling rate. Then, *y(t)* and *x(t)* are input into the Laguerre deconvolution algorithm of order *L* and scale parameter *α*. The Laguerre deconvolution algorithm has the following steps:

1- Create Laguerre functions using their recurrence relations [49]:

$$b_i^{\alpha}(n) = \sqrt{\alpha} b_i(n-1) + \sqrt{\alpha} b_{i-1}(n) - b_{i-1}(n-1) \quad \textbf{(4.4a)}$$

$$b_0^{\alpha}(n) = \sqrt{\alpha^{n-1}(1-\alpha)} \quad \textbf{(4.4b)}$$

$$b_i^{\alpha}(0) = \sqrt{\alpha}\, b_{i-1}(0) \quad \textbf{(4.4c)}$$

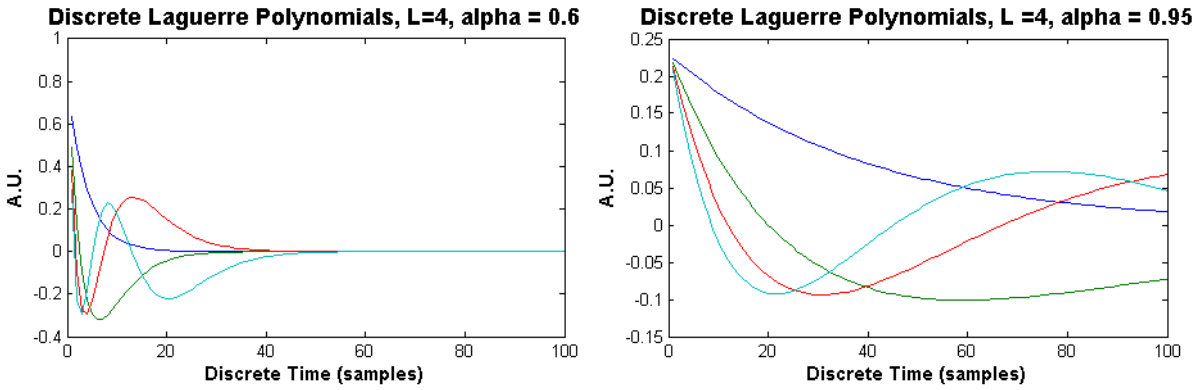

Figure 4-1. Plot of the discrete Laguerre functions of the first 4 orders. 2 scale parameters (0.6 and 0.95) are used to show the effect it has on the functions.

2- the convolution of the Laguerre functions with the IRF is calculated:

$$v_j(t) = b_j(t) * x(t) \quad \textbf{(4.5)}$$

3- The linear minimization problem below is solved for the Laguerre coefficients, *C*:

$$\underset{c}{\operatorname{argmin}} \mid CV - Y \mid \quad \textbf{(4.6)}$$

$$C = [c_0 \quad \dots \quad c_{L-1}] \quad \textbf{(4.7a)}$$

$$V = \begin{bmatrix} v_0(0) & \cdots & v_0(n-1) \\ \vdots & \ddots & \vdots \\ v_{L-1}(0) & \cdots & v_{L-1}(n-1) \end{bmatrix} \quad \textbf{(4.7b)}$$

$$Y = [y(0) \quad \dots \quad y(N-1)] \quad \textbf{(4.7c)}$$

4- The Laguerre coefficients are used to approximate *h(t)*, and the error in the deconvolution is calculated according to equation **4.9**.

$$\hat{h}(t) = \sum_{j=1}^{L} c_j b_j(t) \quad \textbf{(4.8)}$$

$$E = 100 * \frac{\sum |(h_i - \hat{h}_i)|}{\sum (h_i)} \quad \textbf{(4.9)}$$

Given the above algorithm, there remains the choice of the following in its implementation:

1. The choice of scale parameter, α.
2. The choice of approximation order, *L*.

To decide on the choice of the scale parameter, α, a simple method would be to iterate over a range of values and choose the one with the lowest fitting error. Note that this increases computation time significantly compared to choosing a single value of α.

To decide on the choice of *L*, a simulation is carried out as described above at SNR = 50, f_s = 10 GSPS, τ incremented at 400 ps intervals, and α chosen by iterating through values from 0.7 to 0.99 at increments of 0.01. The simulation was rerun at different orders (*L*) of Laguerre functions. The results of this simulation, figure 4-2, show that changing the order from 3 through 7 makes no difference to the fitting error. Thus, there must be another factor dominating the error besides the approximation error. The parameter controlling the error is lifetime dependent. The error as a function of sampling rate is expected to be lifetime dependent as well. To investigate if the limited sampling rate dominates the error, the same simulation is run again, but at SNR = $+\infty$ (no noise) and *L* = 5. The results in figure 4-3, show that the sampling rate greatly influences the error.

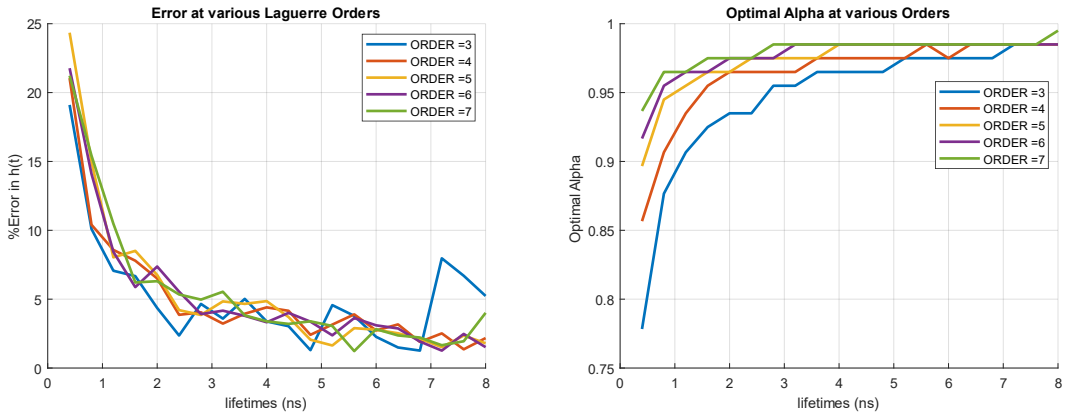

Figure 4-2. **(left)** Error as a function of sampling rate in simulation at *SNR*=50 and f_s 10 GSPS. **(right)** Optimal alpha as a function of lifetime in the same simulation. Optimal alpha is the one which results in the lowest fitting error.

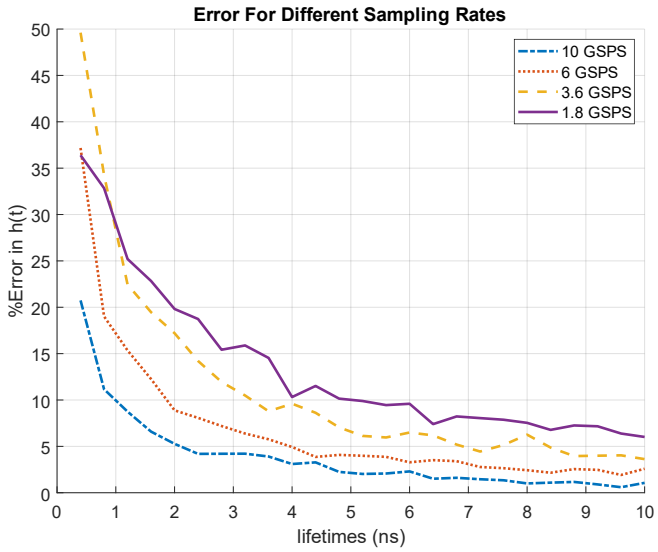

Figure 4-3. Error for different sampling rates, SNR = +∞ (no noise), L = 5

The effect of sampling rate on the error raises the question of whether creating more samples by interpolation would help mitigate the error. To address this question, the algorithm is changed in one aspect: Before starting the Laguerre deconvolution procedure, *y(t)* is linearly interpolated such that it has 2000 points. The number 2000 was chosen to represent 'sufficient sampling'. The simulation for error as a function of L is run again with the interpolation step added, and the results are shown in figure 4-4.

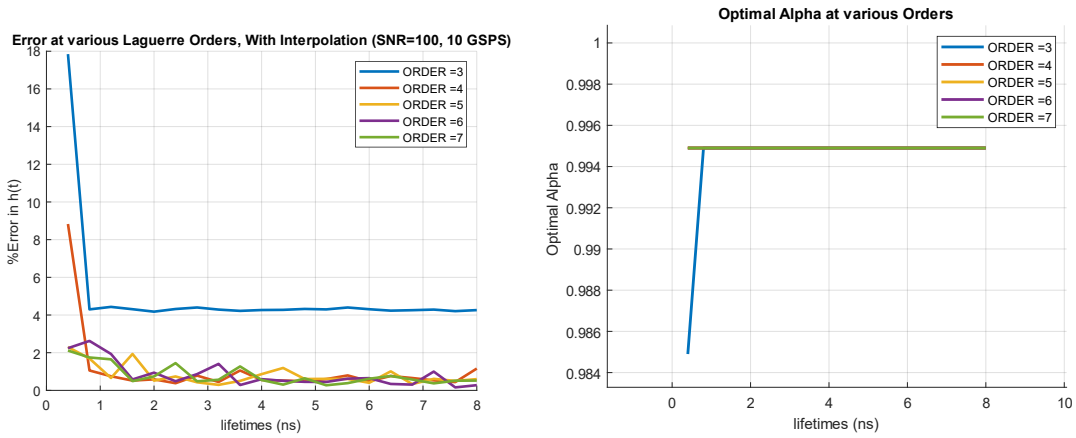

Figure 4-4. **(Left)** Error for different approximation orders when interpolation is used. **(Right)** Optimal alpha with interpolation to within 0.01, found by iterating through alpha values at intervals of 0.01 and finding the one with lowest fitting error

Comparing figure 4-4 to figure 4-3 at 10 GSPS shows that interpolation reduces error. Additionally, it has the effect that regardless of sampling rate or lifetime, a single α value, 0.995, is optimal (within 0.01) for all lifetimes greater than the IRF width. Thus, it with this approach it is not necessary to iterate over alpha values to search for the optimal one.

The function order is chosen to be the minimum number such that increasing the order by 1 causes a reduction of error which is small relative to the expected error in *h(t)*. This is an empirical choice of order to prevent overfitting while keeping approximation error reasonably low. Figure 4-4 shows that 3rd order fitting would introduce significant approximation error. Thus, the order chosen should be at least 4, but not large enough to fit to noise, which would depend on the noise level.

To investigate the effect of sampling rate on error with the interpolation approach, the simulation is run again at lifetime from 400 ps to 6 ns at intervals of 100 ps. The parameters used are: *SNR*=100, *L*=5, α=0.995, with *y(t)* interpolated to 2000 points (*N*=2000). Figure 4-5 shows that if aiming for <2% error in *h(t)*, a sampling rate greater than 3.6 GSPS is required at 100 SNR. However, error spikes up for lifetimes below 500 ps, which is the FWHM of the IRF in the simulation. This raises the question of whether searching for an optimal alpha reduces error significantly at those lifetimes. To address this question, the simulation is run again for lifetimes from 100 ps to 1 ns, with interpolation (*N*=2000), but searching for optimal alpha to within 0.01. Figure 4-6 shows the result of this simulation, which is that the sampling rate defines a lower bound on the lifetimes that can be resolved. Roughly, that lower bound is 3 samples in the duration of one lifetime.

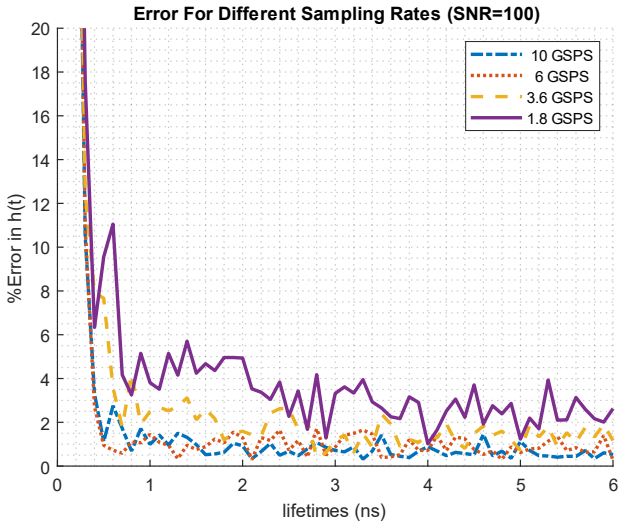

Figure 4-5. Error at different sampling rates with *SNR=100, L=5, α=0.995, N=2000*

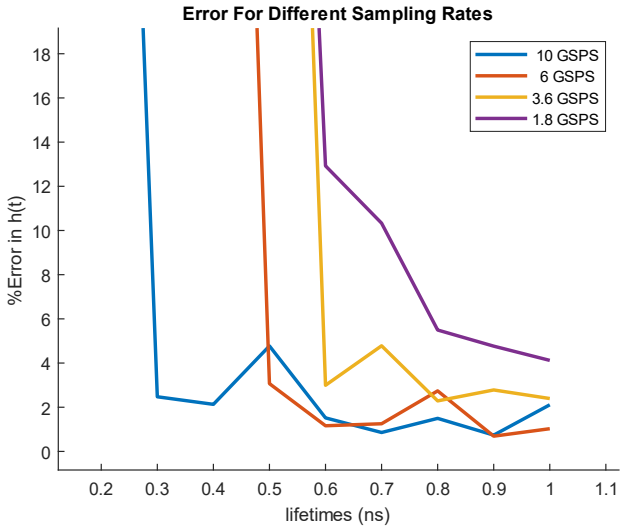

Figure 4-6. Error for different sampling rates at low lifetimes at *SNR=100, L=5, N=2000* but with a searching for optimal α.

Next, the effect of IRF width on the lower limit of what lifetimes can be resolved is investigated. The same simulation as above is performed with the following parameters: *SNR*= $+\infty$ (no noise), L=5, N=2000, f_s=20 GSPS and optimal α searched for, and the IRF FWHM is varied. The result of this simulation, figure 4-7, is that at L=5, the IRF width also places a lower bound on lifetimes that can be resolved, with the shortest resolvable lifetimes being roughly half of the IRF FWHM.

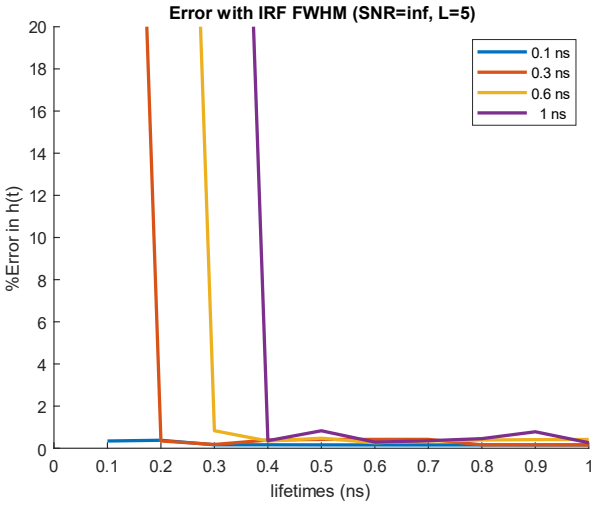

Figure 4-7. Error at different IRF widths. *SNR*= +∞, *L*=5, *N*=2000, f_s=20 GSPS

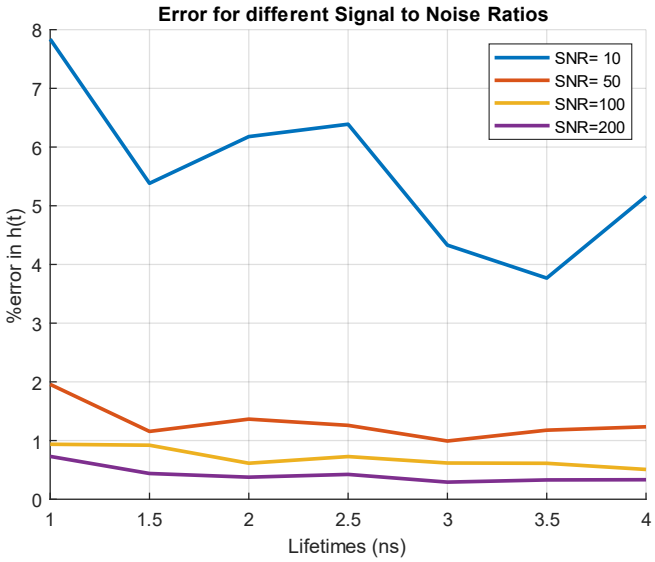

Figure 4-8. Error at different SNR, with *L*=5, *N*=2000, α=0.995, IRF FWHM = 500 ps, f_s = 10 GSPS

Next, the effect of signal-to-noise ratio is investigated. The simulation is run for lifetimes from 1 ns to 4 ns at 500 ps intervals, with 20 repeats for each lifetime. The parameters used are: *L*=5, *N*=2000, α=0.995, IRF FWHM = 500 ps, f_s = 10 GSPS, and varying SNR. Figure 4-8 shows that 50 SNR is sufficient to achieve <2% error in *h(t)*, within the assumptions of this simulation.

One source of noise not considered in the above simulation is quantization noise from analog-to-digital conversion. With a dynamic range of 1V and a signal peak of 50mV, only 5% of the dynamic range of the digitizer would be used, and digitization noise can

be significant. To simulate this scenario, *y(t)* is scaled such that its maximum is 5% of the largest number represented by the given bit depth ($2^{\text{Bit depth}}$-1), and then each sample in *y(t)* is rounded to the nearest integer. The simulation is rerun with lifetimes from 1 ns to 4 ns at 500 ps intervals with the following parameters: *SNR* = 50, *L*=5, f_s = 10 GSPS, α=0.995, IRF FWHM = 500 ps.

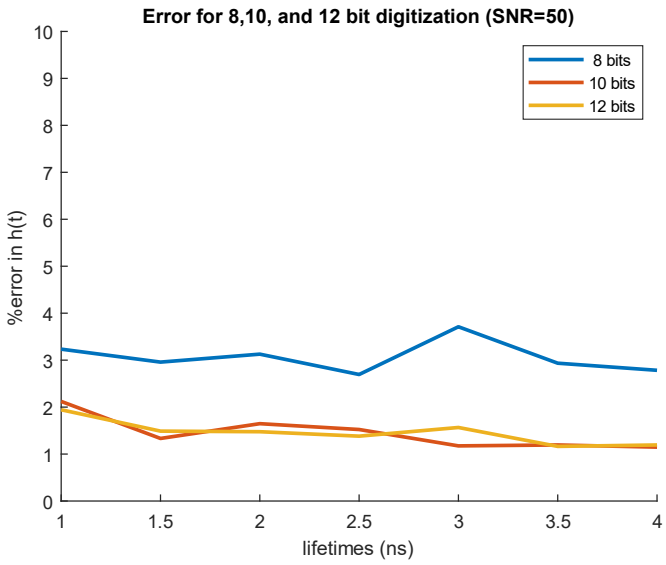

Figure 4-9. Error with different bit depths in simulation with quantization error, when signal peak reaches 5% of digitizer's dynamic range.

When using 8-bits, the bit depth becomes a limiting factor of error. There is no significant difference between using a 10-bit and 12-bit ADC at 50 SNR, using 5% of the dynamic range.

Some limitations of this simulation are listed below:

- Gaussian IRF may not represent actual instrument response. The simulation did not investigate effects of asymmetry in the IRF
- The simulation did not consider different decay mechanics other than a single exponential decay.
- A major assumption is that the IRF is perfectly known (no noise in IRF, no systematic errors). This includes uncertainty in the time offset of IRF relative to rise of *y(t)*. This includes the assumption that the IRF is known at a sufficiently high sampling rate.
- The simulation did not consider situations with low photon counts and high gain, where Poisson noise becomes significant.

The simulation leads to the conclusion that if aiming for <2% error in *h(t)*, one of the requirements is a digitizer with a bit depth greater than 8, and an acquisition SNR greater than 50. At sampling rates of 3.6 GSPS, Laguerre deconvolution will fail for lifetimes

less than 600 ps, while for sampling rates of 10 GSPS, that limit is extended to 300 ps. To resolve such small lifetimes, both a narrower instrument response and a faster sampling rate are required. One of those conditions alone is not enough to resolve short lifetimes (below 300 ps).

4.2. Phasor approach for Hyperspectral TRF

Laguerre deconvolution only retrieves an approximation of the intrinsic fluorescence, but not the fluorescence lifetimes. For classification purposes, one option is to stop at this stage and use the Laguerre coefficients to describe the fluorescence decays and use those coefficients for classification of biological tissue. The problem with this approach is that the coefficients do not translate directly to a physical representation as intuitive as the lifetime. On the other hand, fluorescence lifetimes can be attributed to individual chemicals and changes in their concentration or environment.

We propose using the phasor approach to analyze the hyperspectral data. This approach describes the fluorescence as a sum of components which contribute differently at each wavelength according to their emission spectra. To illustrate how phasor analysis can be applied to hyperspectral time-resolved data, hyperspectral TRF data is measured using system A, with targets being mixtures of dyes at varying concentrations. The phasor approach is applied to the mixtures to find lifetimes, relative concentrations and individual spectra from a mixture of 2 fluorophores.

The dye preparation materials are identical to those in chapter **3.4.3**. That is, FL, C6, and 9CA in anhydrous ethanol at concentrations of 1 mM. Mixtures of Fluorescein (FL)+Coumarin-6 (C6), and Fluorescein + 9-Cyanoanthracene (9CA) were prepared by pipetting volumes in the ratios of 1:0, 3:1, 1:1, 1:3 and 0:1. Mixtures of these 3 dyes were similarly prepared in volumetric ratios of 1:1:1, 2:1:1, 1:2:1 and 1:1:2.

The spectra of the chosen dyes individually, excited at 355 nm and measured with a spectrometer, are shown in figure 4-10. They have significant spectral overlap. Thus, given a mixture of Fluorescein and Coumarin-6, it would be difficult to resolve the spectrum of each fluorophore individually with only the spectral measurement. This makes these mixtures a non-trivial case of applying phasor analysis to separate 2 components.

At each wavelength, the measured decays, $y(t)$¸ are normalized to have an area of 1. Then, G and S are calculated from the highest frequency component in the discrete Fourier transform of the measured decays, $y(t)$, according to equations **2.12** and **2.13**. A straight-line fit is performed on the GS plane, and the intersection of this line with the semicircle is found using equations **4.10,** where m and b are the slope and intercept of the straight-line fit respectively. Figure 4-11a shows the result of this method in a mixture of FL and C6. The straight line lies outside the semicircle and does not reflect the GS coordinates of the 2 components.

$$\Delta = \sqrt{-4b^2 - 4bm + 1} \quad \textbf{(4.10a)}$$

$$G_{1,2} = \frac{\pm\Delta - 2bm + 1}{2(m^2+1)} \quad \textbf{(4.10b)}$$

$$S_{1,2} = mG_{1,2} + b \quad \textbf{(4.10c)}$$

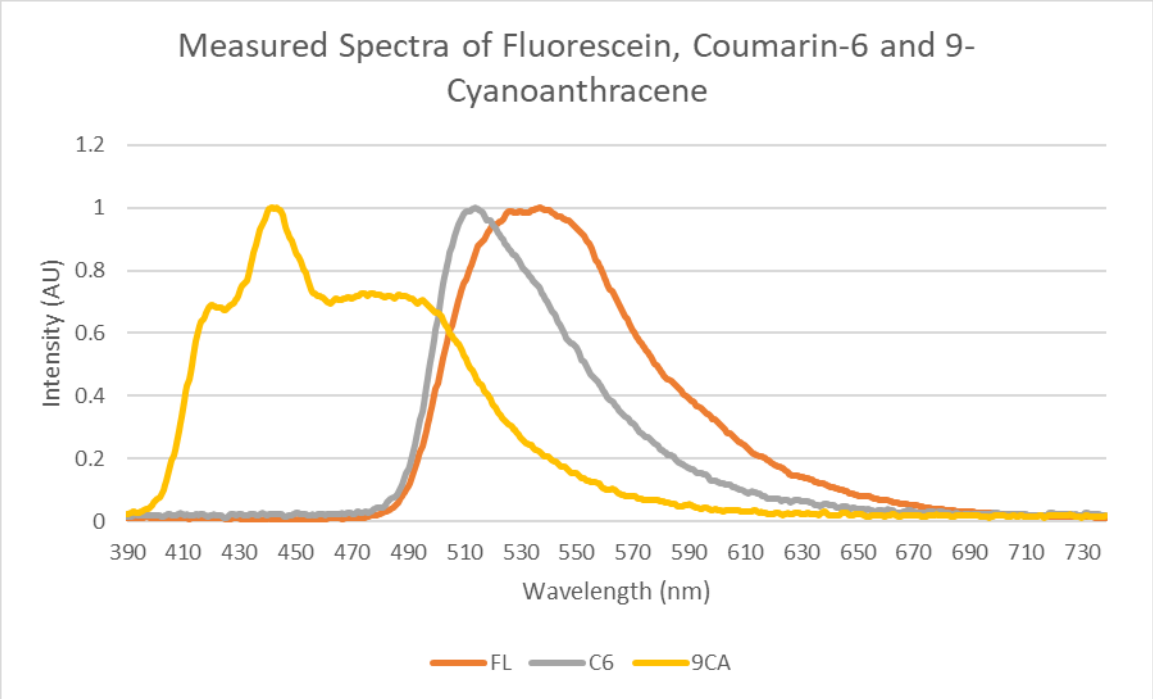

Figure 4-10: Emission spectra of Fluorescein, Coumarin-6 and 9-Cyanoanthracene.

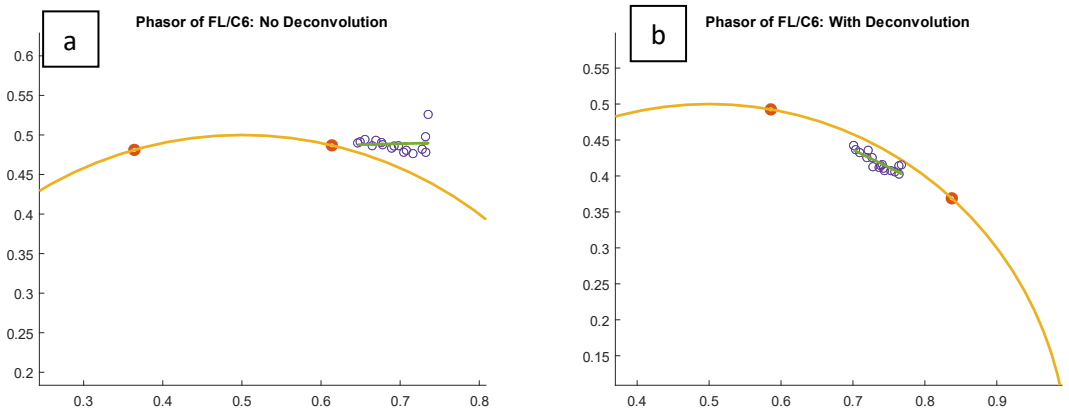

Figure 4-11. Phasor representation of mixture of C6/FL, without deconvolution (**a**), and with deconvolution (**b**).

Figure 4-11a highlights the need for deconvolution in the hyperspectral unmixing approach. In literature, the following methods are available to correct for the instrument response:

1) Corrections in the Fourier domain, given the IRF [37].
2) Corrections using a calibration dye, given a dye with a known lifetime [51].

We propose using the deconvolved decays from Laguerre deconvolution as the input to the phasor analysis. The Laguerre deconvolution takes care of denoising and correcting the instrument response. However, it comes with the tradeoff of approximation error, as well as carrying over any uncertainty in the IRF. Laguerre deconvolution with interpolation is applied as shown in section **4.1.** $L = 6$ and α=0.995, N=2000 is used for all subsequent deconvolutions. Figure 4-12 shows the hyperspectral phasor representation of fluorescein after deconvolution. Figure 4-11b shows that using *h(t)* instead of *y(t)* as the input for the phasor unmixing method gives the expected line inside the universal semicircle.

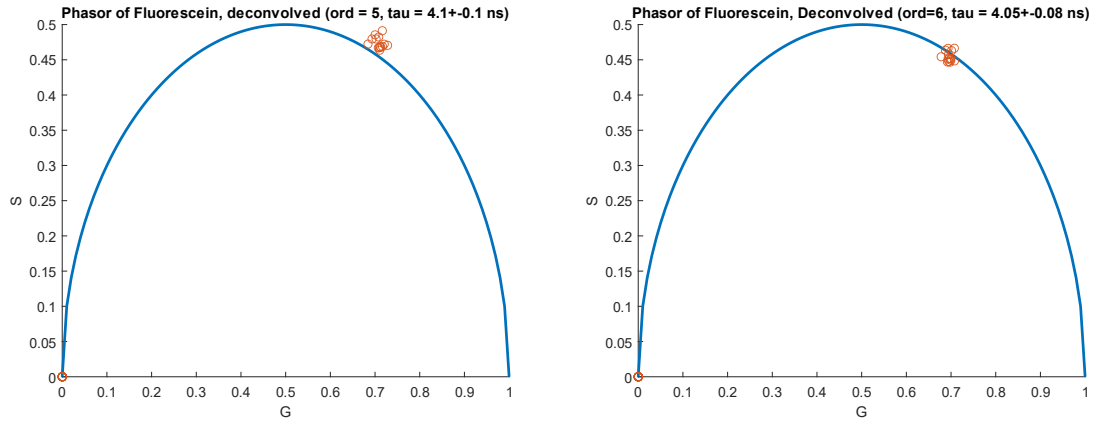

Figure 4-12. Phasor representation of deconvolved fluorescein decays at $L=5$ and $L=6$.

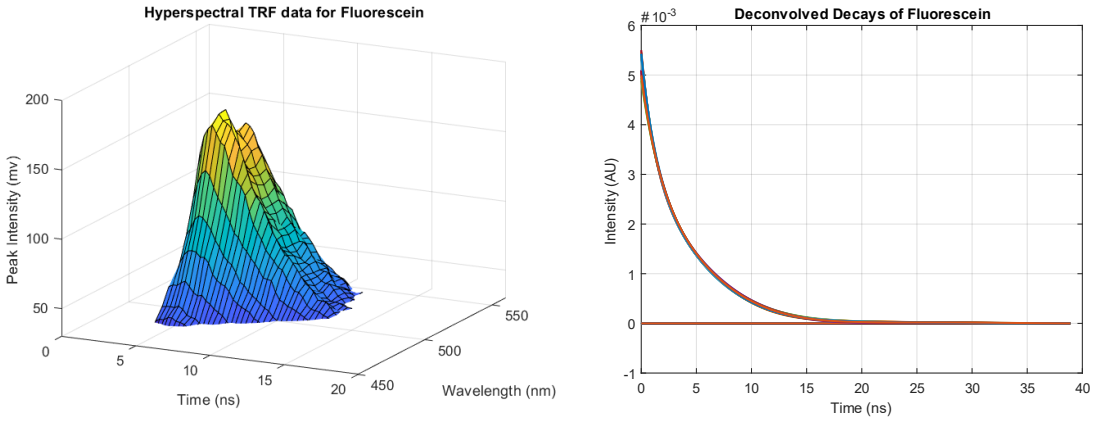

Figure 4-13. **(Left)** Time domain hyperspectral TRF data from fluorescein. **(Right)** Deconvolved hyperspectral decays.

After unmixing the 2 component's coordinates, *(G_1, S_1)* and *(G_2, S_2)*, the individual lifetimes are calculated using equation **4.11**. Then, for each phasor point, distance from the component's coordinates is calculated (**4.12a),** and that is used to calculate relative photon contributions (**4.12b,c,d).** This procedure is repeated for mixtures of varying concentrations, and the results are summarized in the table 4-1.

$$\tau_{1,2} = \frac{1}{\omega}\frac{S_{1,2}}{G_{1,2}} \quad \textbf{(4.11)}$$

$$d_{1,2} = \sqrt{\left(S - S_{1,2}\right)^2 + \left(G - G_{1,2}\right)^2} \quad \textbf{(4.12a)}$$

$$a_{1,2} = \frac{d_{2,1}}{d_1 + d_2} \quad \textbf{(4.12b)}$$

$$\%C_1 = \frac{\sum_{i=Wavelengths} I_i * \frac{a_1 \tau_1}{a_1\tau_1 + a_2\tau_2}}{\sum_{i=Wavelengths} I_i} \quad \textbf{(4.12c)}$$

$$\%C_2 = 1 - \%C_1 \quad \textbf{(4.12d)}$$

Table 4-1. Measured lifetimes and percentage photon contributions from mixtures of 2 dyes

Fluorophore	**Measured lifetime, τ_1(ns)**	**Measured lifetime, τ_2(ns)**	**% of total photon counts**
9CA	11.07 ± 0.02	N/A	100%
C6	2.74 ± 0.04	N/A	100%
FL	4.10 ± 0.02	N/A	100%
25% (FL / 9CA) 75%	4.16 ± 0.9	11.23 ± 0.1	15% - 85%
50% (FL / 9CA) 50%	3.73 ± 0.9	11.17 ± 0.2	17% - 83%
75% (FL / 9CA) 25%	3.76 ± 0.2	11.34 ± 0.1	26% - 74%
25% (FL / C6) 75%	4.52 ± 0.8	2.57 ± 0.3	19% - 81%
50% (FL / C6) 50%	4.61 ± 0.4	2.71 ± 0.2	22% - 78%
75% (FL / C6) 25%	4.28 ± 0.3	2.45 ± 0.2	34% - 66%

The results in table 4-1 show that this approach can reliably unmix the fluorescence lifetimes under the assumption that there are 2 fluorophores which individually have exponential decays. However, uncertainty can become quite large when one fluorophore contributes significantly more than the other. This is seen in the case of FL and 9CA mixtures where the uncertainty in Fluorescein lifetime is greater than 20%. Additionally, the percentage contribution calculation only counts wavelengths the TRF system can detect (370 to 550 nm for system A). Since wavelengths outside this range are not

counted in the emitted photon count, so %contributions cannot be translated to relative concentrations even if the quantum yield is known. However, this method can still indicate changes in relative concentrations from one target to the next. If the emission spectra as well as the quantum yields of the fluorophores being measured are known, then relative concentrations can be measured. Problems in the experimental setup include not controlling the pH of fluorescein, which can have a large influence on its lifetime. Also, C6/9CA mixtures were not made, although they might have given additional data on how this approach would work when the difference in lifetimes is large (2.6 vs 11.0 ns). Additionally, the number of repeats is low, at 3 repeats for each mixture.

Some challenges in biological tissue will be that individual fluorophores may have bi-exponential decay models. Additionally, 3 or more fluorophores may be present, resulting in a curved line in phasor space. To investigate this scenario, the same approach as above is applied to mixtures of 3 dyes. The same 3 dyes (FL, C6, 9CA) were used, in ratios of 1:1:1, 2:1:1, 1:2:1, and 1:1:2 (by volume).

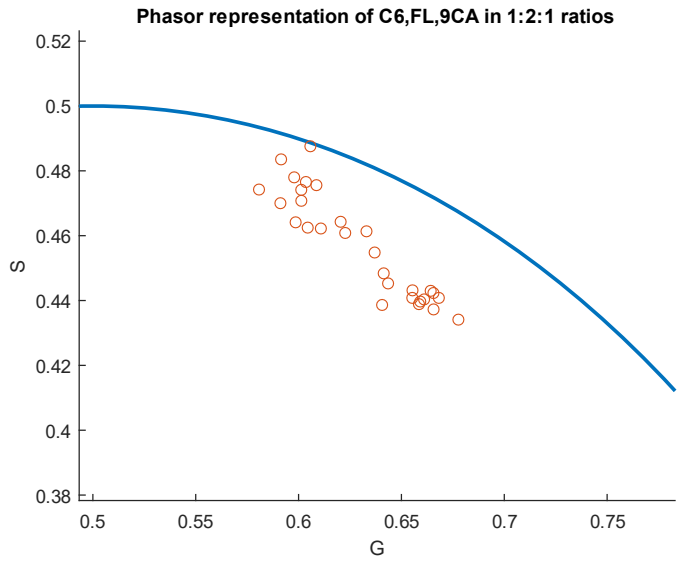

Figure 4-14. Phasor representation of decays from a mixture of 3 dyes.

The phasor picture does not allow simple separation into 3 components. This will be a difficulty that arises when looking at TRF data from biological tissue.

4.3. Spectral-Temporal Model

The phasor approach did not succeed in unmixing 3 components. Thus, a different approach is taken, where both the spectral and phasor data are fit to a model. A Gaussian-mixture model is proposed, where each fluorophore has a Gaussian-shaped emission spectrum with a center wavelength λ_i and a decay profile with a unique phasor coordinate (G_i, S_i). Each fluorophore has a different relative amplitude A_i. The minimization problem in equation 4.13 is solved for the peak wavelengths and G, S coordinates.

$$\min: \frac{\left(I_{fit}(\lambda)-I(\lambda)\right)^2}{\sigma_I} + \frac{\left(G_{fit}(\lambda)-G(\lambda)\right)^2}{\sigma_G} + \frac{\left(S_{fit}(\lambda)-S(\lambda)\right)^2}{\sigma_S} \quad \textbf{(4.13a)}$$

$$G_{fit}(\lambda) = \sum_{i=1}^{3} f_i\,(\lambda)\, G_i \quad \textbf{(4.13b)}$$

$$S_{fit}(\lambda) = \sum_{i=1}^{3} f_i\,(\lambda)\, S_i \quad \textbf{(4.13c)}$$

$$I_{fit}(\lambda) = \sum_{i=1}^{3} I_i(\lambda) = \sum_{i=1}^{3} \frac{A_i}{\sigma_i\sqrt{2\pi}} e^{-\frac{(\lambda-\lambda_i)^2}{2\sigma_i^2}} \quad \textbf{(4.13d)}$$

$$f_i(\lambda) = \frac{I_i(\lambda)}{\sum_{i=1}^{3} I_i(\lambda)} \quad \textbf{(4.13e)}$$

f_i are the fractional intensity contributions of each fluorophore. $\sigma_I, \sigma_G, \sigma_S$ represent the standard deviation of the measured values (*I, G, S).* The minimization routine solves for $\{A_i, \lambda_i, \sigma_i, S_i, G_i\,; i = 1,2,3\}$, for a total of 15 parameters to approximate both the spectral and lifetime information. The intensity used for this model was obtained from the integrals of the hyperspectral decays, divided by the PMT's spectral sensitivity at each wavelength. This sensitivity is obtained in the same procedure as in chapter 3.4.3.

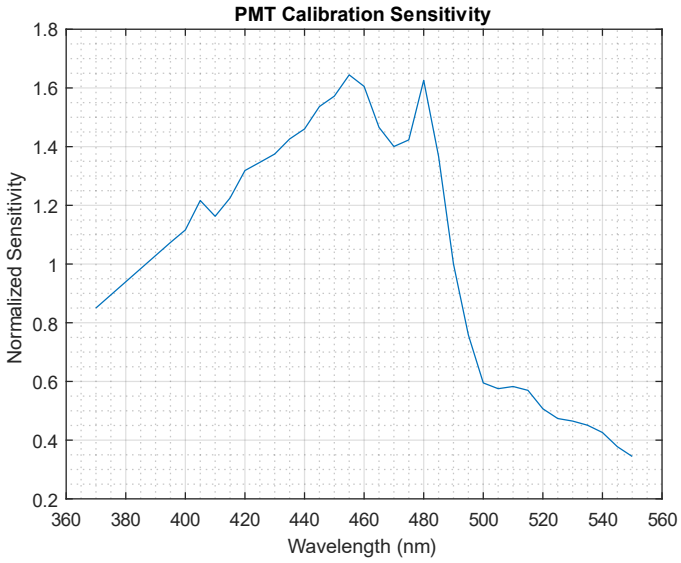

Figure 4-15. System A's PMT spectral calibration calculated with different dyes, with procedure shown in chapter 3.4.3. The dyes used for this calibration were 9CA, FL, and C6 at 1 mM. The region 370 to 400 nm was obtained by linear extrapolation.

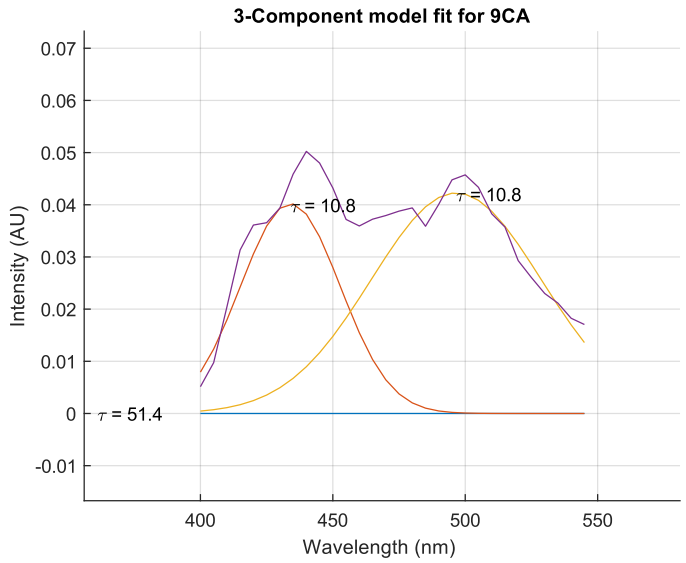

Figure 4-16. 3-component spectral and temporal fit of hyperspectral data from 9-cyanoanthracene. One of the components has negligible amplitude and fits to noise in the phasor domain.

When the Gaussian-mixture model is applied to the 9CA hyperspectral decays, 2 components are used to fit the spectral data and one component fits to noise in the phasor domain, as shown in figure 4-16. To prevent this, an extra step was added to the algorithm: If one of the components has a fractional contribution below 1%, then that component is discarded, and the fit is redone with fewer components. Figure 4-17 shows that the model gives reasonable results on single dyes. However, when the model is applied to mixtures of dyes, it fails to unmix their lifetimes correctly. The retrieved lifetimes from the mixtures are dependent on concentration, as shown in figure 4-19. For example, the lifetime obtained for fluorescein is not the expected 4.0 n; It is skewed towards the lifetime of the other component, in this case 9CA. The model also fails to see the mixture of C6 and FL as having 2 fluorophores, possibly because their emission spectra are similar.

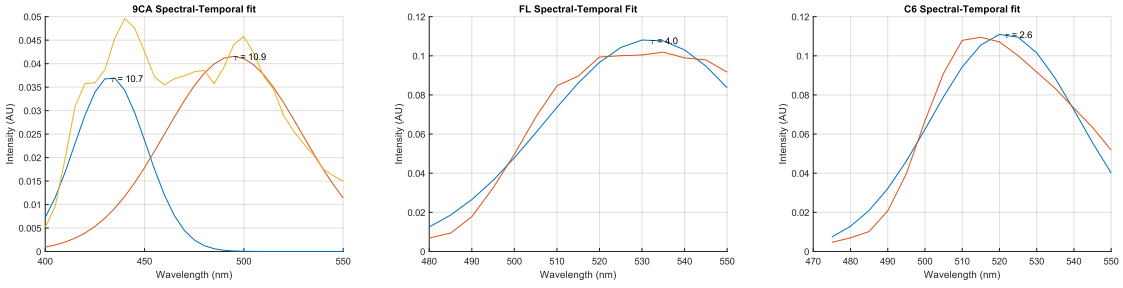

Figure 4-17. Spectral-Temporal fit of individual fluorophores with gaussian mixture model eliminating low amplitude components.

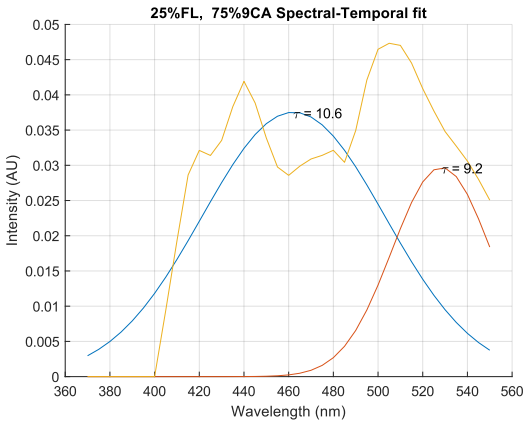

Figure 4-18. Example of spectral-temporal unmixing applied to mixture of FL and 9CA with volume ratios of 1:3.

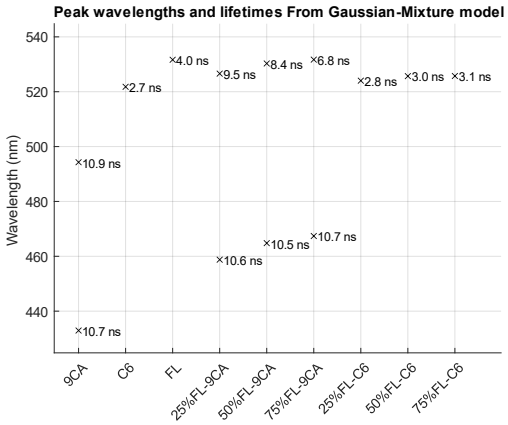

Figure 4-19. Fluorescence lifetimes and peak wavelengths from spectral-temporal fits. The key features are that extracted lifetimes and peak wavelengths are influenced by changes in relative concentrations, and that the model fails to un-mix FL and C6 lifetimes and spectra.

4.4. Conclusion

The implementation of Laguerre deconvolution differs from previous work such as [38] in the aspect that the decays are interpolated to have the same number of samples every time. The simulations showed that this reduces dependence on the scale parameter and lowers the effect of limited sampling rate on the error. The results lead to the conclusion that hyperspectral phasor unmixing on deconvolved decays works reliably for mixtures of 2 fluorophores. The phasor unmixing method was not successful for 3 components. This is partly because the 9CA signal significantly dominated the other 2 components. However, it is also due to the fact that the straight-line fit method in phasor space cannot be used to obtain 3 components. The Gaussian-mixture model failed at

unmixing fluorescence lifetimes correctly. A major reason for this is that emission profiles are not Gaussian-shaped and are usually asymmetric. Another reason is that the spectra are truncated due to the limited wavelength range of the AOTF. This leads the algorithm to make wrong assumptions about the intensity outside the recorded wavelength range. Lastly, the model has too many parameters for the given data points(15 parameters for 3 components), which leads the fit to local minima depending on the initial conditions used.

Chapter 5

Discussion and Conclusions

Having verified the acquisition and analysis procedures on dyes, the next step for an optical biopsy study is data collection from a cancerous target. A DR-TRF case study is performed on an *ex-vivo* sample diagnosed to be a glioblastoma. The data from this sample is compared to an older dataset from an *ex-vivo* DR-TRF study on glioblastomas and meningiomas. 2-component phasor unmixing as well as exponential fits are used to describe the hyperspectral TRF data. Unanswered questions from the datasets reveal the remaining obstacles and next steps to reach a conclusive optical biopsy study.

5.1. Brain Cancer Case Studies

The first dataset was obtained from a single tissue sample from a patient suspected of having brain cancer. The sample was a lump with estimated dimensions of 1-2 cm in length and 0.5-1 cm in depth. It was taken directly from the surgery room, labelled as "right temporal tumor". DR-TRF measurements were taken with system A on 6 points along the surface of the tissue, with 3 repeats per point. After the DR-TRF measurements were taken, the sample was passed to a pathologist who diagnosed the tissue as a glioblastoma. The points were not labelled with a dye, and thus no co-registration was made between the pathologist's diagnosis and the probed points. TRF measurements were taken at a PMT voltage of 2350-2400V, and laser power was measured as 2.9 mW.

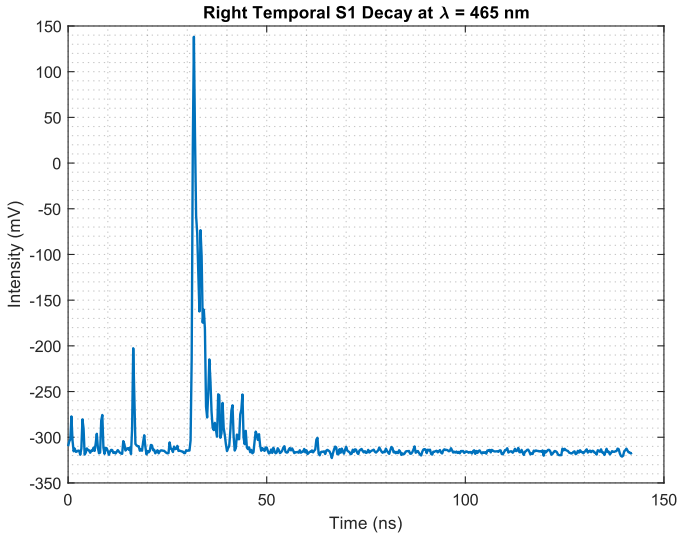

Figure 5-1. Example of a measured decay from Right Temporal sample at 465 nm. This is before the 11 repeats were averaged.

Noise spikes of unknown origin are observed in the time-domain data, such as in figure 5-1. Their amplitude is consistent across the TRF wavelength range. This noise was not observed in the dye measurements used to verify the system's temporal response. It may due to shot noise as a consequence of low photon count from the fluorescence.

Information that can be extracted from this sample includes fluorescence lifetime as a function of wavelength, emission spectrum and reflectance as a function of wavelength at different SDD.

To obtain average fluorescence lifetime as a function of wavelength, the TRF data is passed through Laguerre deconvolution as in chapter 4.1 to obtain *h(t)*. Wavelengths with peak voltage below 100 mV were truncated. A high truncation voltage was chosen because at lower amplitudes, the spikes shown earlier would dominate the signal. The average lifetimes were calculated from *h(t)* for S1 to S6 using equation **5.1**, and the results are plotted in figure 5-2. One feature of these average lifetimes is that they change continuously as a function of wavelength, as opposed to figure 3-13, where the lifetime is constant as a function of wavelength. The continuous change is due to the change in relative contributions of the present fluorophores as a function of wavelength, which changes continuously according to the emission spectra.

$$\tau = T \frac{\sum_{n=0}^{N-1}(n+0.5)\, h(n)}{\sum_{n=0}^{N-1} h(n)} \qquad \textbf{(5.1)}$$

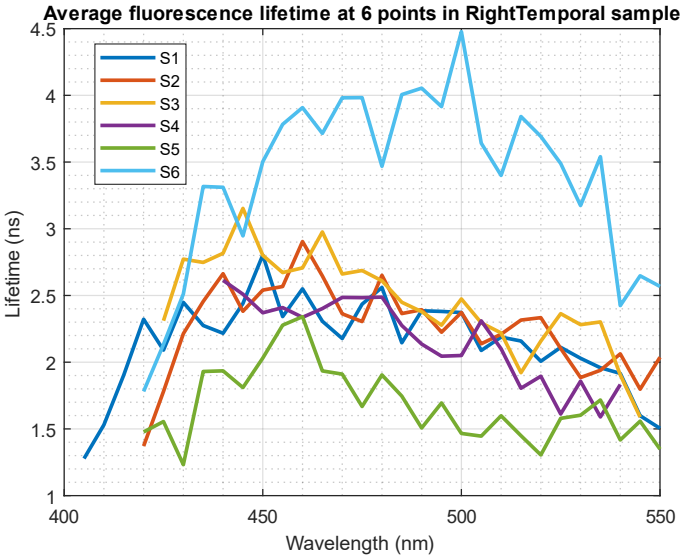

Figure 5-2. Average fluorescence lifetime as a function of wavelength for Right Temporal sample

It is desirable to attribute the lifetimes over the wavelength range to individual fluorophores. To do that, the phasor analysis method from chapter 4.2 is applied, by fitting a straight line in phasor space. This results in 2 lifetimes for each point on the

'Right Temporal' sample, as shown in figure 5-3. The emission spectra are obtained by finding the integrals of the measured decays and normalizing by dividing by the sensitivity as a function of wavelength. The sensitivity for system A was found in section 3.4.3 and is shown in figure 3-10. Error bars are obtained from the standard deviation in the repeats for each of the 6 sample points along the tissue. The resulting corrected spectrum is shown in figure 5-4. Lastly, reflectance as a function of wavelength is plotted, shown in figure 5-5. The reflectance measurements are after background subtraction, which takes place as part of the acquisition procedure, similarly to the procedure in figure 3-4.

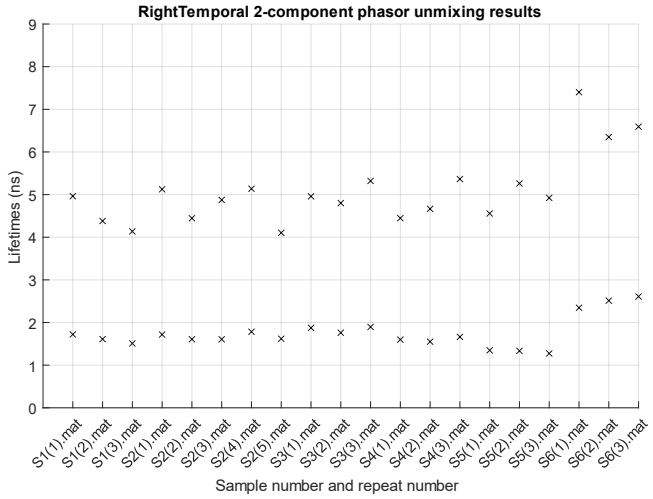

Figure 5-3. Lifetimes obtained from 2 component phasor unmixing of deconvolved decays from the 'Right Temporal' sample

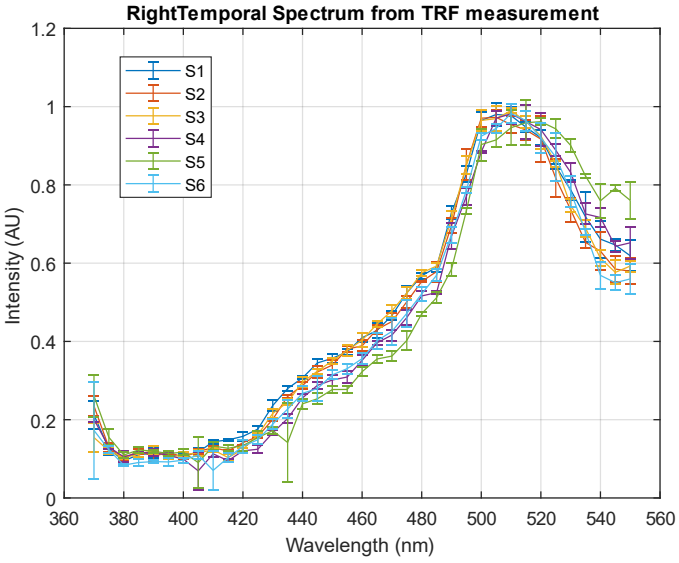

Figure 5-4. Emission spectra of the 6 points on the Right Temporal sample, normalized to have a maximum of 1.

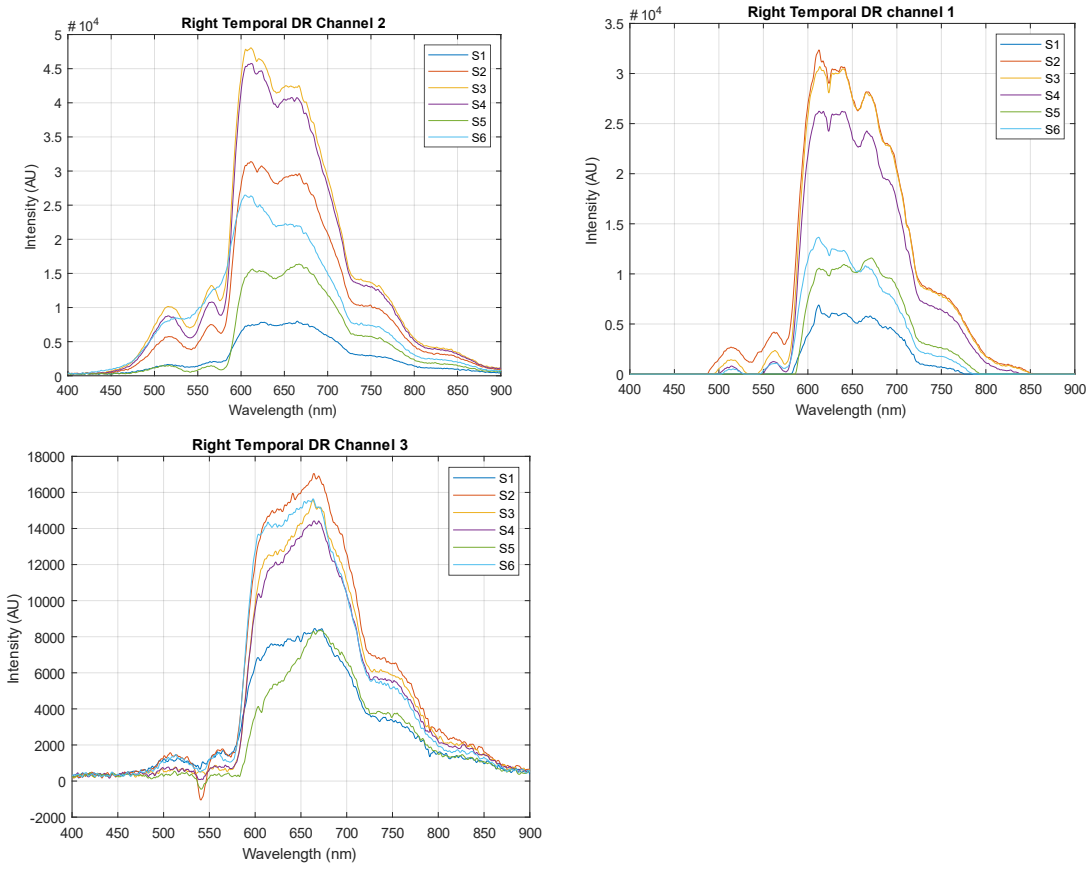

Figure 5-5. Spectrometer measurements of reflected broadband light source at each SDD.

To assess the validity and reproducibility of the DR-TRF measurements, the results from the 'Right Temporal' sample are compared with a previous *ex-vivo* DR-TRF study with high-grade glioma and meningioma samples. The acquisition procedure for this dataset (#2) is outlined in [52]. This dataset has measurements from 14 patients, labelled P01 to P14. Of those patients, 3 were meningioma cases and 5 were high-grade glioma (HGG) cases. Dataset 2 was obtained using system A with slightly different equipment: A 40 GSPS, 8-bit oscilloscope was used for digitization. The fiber probe used is also different. TRF measurements were taken at different points and with differing number of repeats for each patient. The PMT voltages used range from 2300-2400V. The signal to noise is lower than the first dataset. The spectra were calculated from the integrals of the decays at each wavelength and corrected by calibration curve given in figure 5-6. Lifetimes as a function of wavelength were calculated by Laguerre deconvolution followed by equation 5.1, similarly to the first dataset. The spectral and lifetime results are shown in figure 5-7.

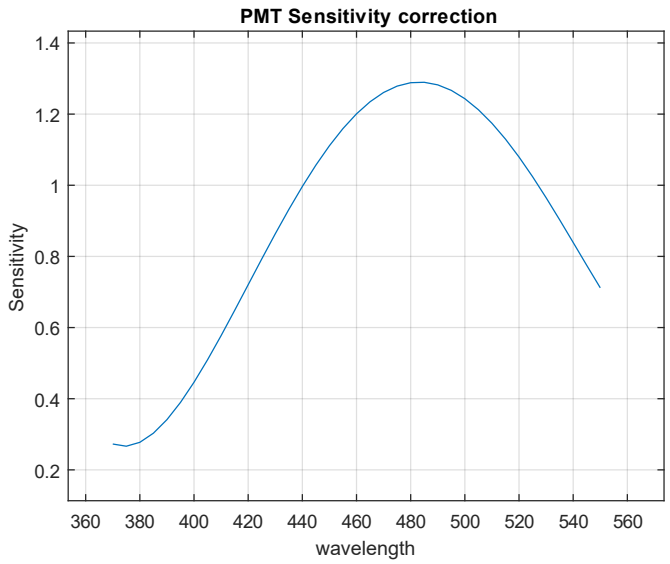

Figure 5-6. Provided sensitivity correction of detector for data set 2.

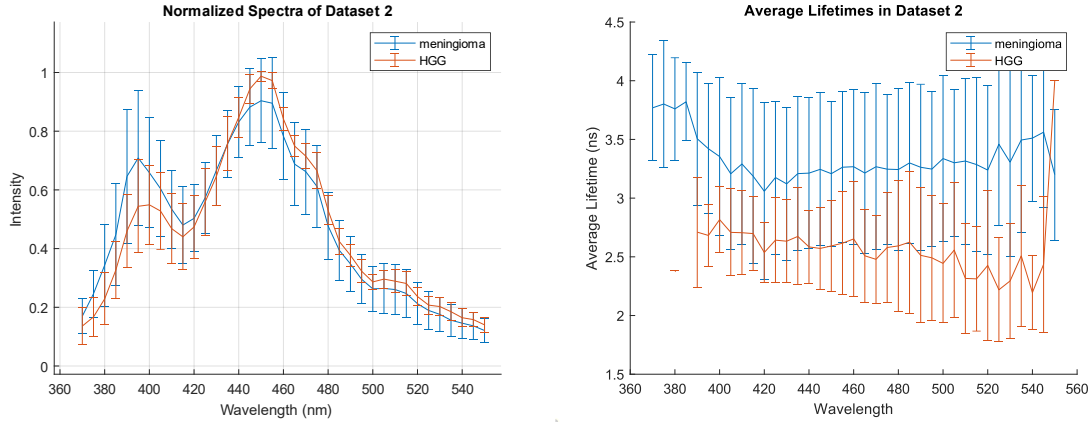

Figure 5-7. **(left)** Normalized and corrected spectra of meningioma and HGG patients from data set 2. **(right)** Average lifetime as a function of wavelength for meningioma and HGG in data set 2. Error bars equate to standard deviation of repeats.

5.2. Case Study Discussion

Figure 5-2 suggests that there are at least 3 fluorophores with significant contribution in the wavelength range in the 'Right Temporal' sample. That is because the lifetime increases with wavelength between 400 nm to 450 nm, then decreases moving from 450 to 550 nm. 2 sample points stand out: Sample 6 has a significantly longer lifetime in the 450-540 nm range than the other sample points. Sample 5 has a significantly shorter lifetime in the 470-520 nm range. This raises the questions of whether S5 and S6 are the only samples that the pathologist classified as a glioblastoma, or was the whole tissue a

glioblastoma and these points stand out for another reason? This question can be addressed if there is co-registration between the pathologist's diagnosis and the exact location that was probed

Another question that arises from figure 5-2 is whether the changes in the lifetime are due to one of the components being more dominant, or a change in lifetime of the individual fluorophores. Figure 5-3 suggests that in sample #6, the individual fluorophores had an increase in lifetime, while in sample#5, the fluorophores do not have a significantly different lifetime compared with the other sample points. Thus, the change in lifetime must be due to an increased concentration of the shorter lifetime component. Figure 5-4 reinforces this conclusion since sample #5 has significantly greater emission in the longer wavelengths (520-550 nm), which is where the lifetime is at its lowest. This exemplifies the usefulness of analyzing decays in terms of components despite the multiple simplifications in the 2-component phasor model.

The DR data in figure 5-5 is difficult to interpret due to there being 3 SDDs, and thus it is not straightforward to interpret if scattering was increased or decreased without a calibration. S1 and S5 have lower intensity than the other sample points at all wavelengths, but this may not be due to greater absorption, but rather to change in light levels reaching the tissue, since the measurements were not normalized against the source intensity. The issues with the DR measurement are summarized below:

1) It needs a calibration to translate the 3 reflectance measurements to μ_s and μ_a
2) It needs a reference measurement to correct for changes in light source intensity and detector integration time.
3) It needs to save the background light measurement in order to verify which parts of the curve may be due to changes in background during the measurement.
4) The channels need to be labelled with their corresponding source-to-detector distances (SDD). In this fiber, the SDD is 0.32 mm, 0.64 mm, and 1.5 mm.

Although background subtraction was carried out, as in the acquisition process shown in chapter 3.3, any variance in the background during the acquisition time may cause dips in the intensity. The dip at 540 nm in figure 5-6 is suspected to be due to due to error in the background subtraction from fluctuations in detected background levels.

In dataset 2, the trend of fluorescence lifetimes is similar to dataset 1, with a decreasing lifetime going from 450 nm to 550 nm. However, the decrease in lifetime at wavelengths below 450 nm is not observed in dataset 2. HGG shows lower fluorescence lifetime than meningioma at all wavelengths. However, the standard deviation in lifetime across repeats is greater than 1 ns, which makes the difference between HGG and meningiomas only around 1 standard deviation. Lowering standard deviation across repeats should be a priority for future studies. One of the issues with using average lifetime obtained after Laguerre deconvolution is the problem of overfitting, such as in shown in figure 5-8**.** A rise in the tail of the decay due to fitting to noise can cause a gross increase in the calculated average lifetime.

The emission spectra in dataset 2 differ significantly from dataset 1. Dataset 2 shows 2 prominent peaks around 400 nm and 450 nm, while dataset 1 shows one prominent peak around 520 nm. Fluorescence at a peak of 400 nm is expected from collagens such as collagen type I. Fluorescence at 460 nm is expected from NAD(P)H and fluorescence around 520 nm is attributed to flavins such as FMN and FAD [53]. It is likely that the difference between the spectra of the datasets is due to the difference in calibration curves used for detector sensitivity, or differences in collection efficiency as a function of wavelength between dataset 1 and 2. It is also possible that there is a background fluorescence component in the system due to a lens or the fiber and that dominated the signal in dataset 1. To confirm this, background measurements should be taken at identical PMT voltage and probe position but without the tissue as a target.

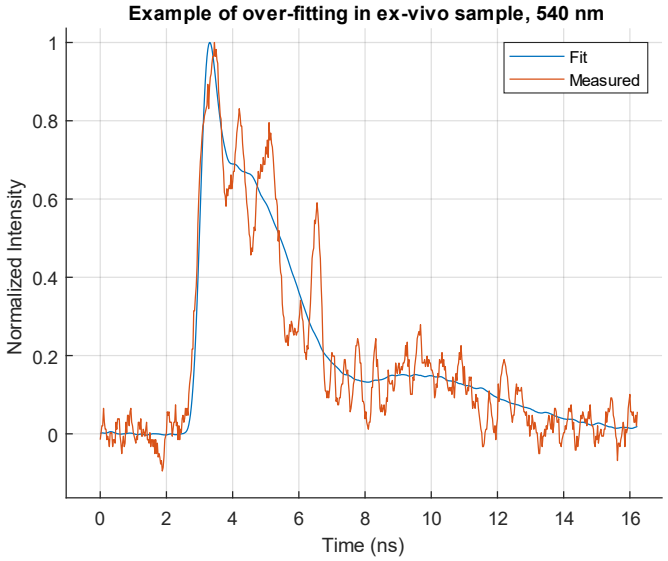

Figure 5-8. Example of a Laguerre fit to a decay from dataset 2 exhibiting overfitting.

The datasets above shed some light on the next steps needed for the DR-TRF instrument to achieve a more conclusive optical biopsy study. Firstly, it is necessary to save the background for both the DR and TRF measurements. The lack of a background measurement makes it hard to know if a feature is due to the tissue sample or not. In the case of DR, that includes dips in the measured reflectance which could be due to fluctuation in the collection of room light. Secondly, it is important to co-register measured points with the pathologist. In invasive cancers such as the glioblastoma in dataset 1, it may not be the case that all 6 points on the tissue are glioblastoma cells. If all 6 measurements are treated as characteristic of glioblastoma cells, then the deviation in the optical properties of the glioblastoma group will be large, making it hard to reach conclusions about differences between cancers and normal tissue. Thirdly, the DR measurements should be calibrated such that optical transport parameters are obtained. This will make finding trends easier than looking at reflectance at 3 different SDDs.

5.3. Closing Remarks

The DR-TRF measurement on the glioblastoma sample shows what the next steps should be to achieve a conclusive optical biopsy study. The most important steps that were missing were the lack of co-registration, background measurements, and DR calibration. We developed a fast method of unmixing fluorescence lifetime components using Laguerre deconvolution and phasor analysis. However, the limitation of this approach is that it assumes there are 2 components which are single exponential. Despite this limitation, this unmixing approach was useful in the tissue case study in determining whether a change in average lifetimes is due to differences in relative concentrations or changes in lifetimes of individual fluorophores. A multi-exponential fitting approach may also be used to carry out such an analysis, but the result may depend greatly on initial parameters and number of components. The improved sampling rate and automation of the DR-TRF instrument is expected to allow easier resolution of time-domain fluorescence information. We hope that the limitations of the preliminary study in this thesis acts as a guide for a future optical biopsy study.

BIBLIOGRAPHY

1. Field, Melvin, et al. "Comprehensive assessment of hemorrhage risks and outcomes after stereotactic brain biopsy." *Journal of neurosurgery* 94.4 (2001): 545-551.
2. Nie, Zhaojun, et al. "Integrated time-resolved fluorescence and diffuse reflectance spectroscopy instrument for intraoperative detection of brain tumor margin." *IEEE Journal of Selected Topics in Quantum Electronics* 22.3 (2015): 49-57.
3. J. R. Lakowicz, Principles of fluorescence spectroscopy, 3rd editor, Springer, New York, 2006.
4. De Bonis, Pasquale, et al. "The influence of surgery on recurrence pattern of glioblastoma." *Clinical neurology and neurosurgery* 115.1 (2013): 37-43.
5. Sun, Yinghua H., et al. "Fluorescence lifetime imaging microscopy for brain tumor image-guided surgery." *Journal of biomedical optics* 15.5 (2010): 056022.
6. Pifferi, Antonio, et al. "Spectroscopic time-resolved diffuse reflectance and transmittance measurements of the female breast at different interfiber distances." *Journal of biomedical optics* 9.6 (2004): 1143-1152.
7. Ge, Zhengfang, Kevin T. Schomacker, and Norman S. Nishioka. "Identification of colonic dysplasia and neoplasia by diffuse reflectance spectroscopy and pattern recognition techniques." *Applied spectroscopy* 52.6 (1998): 833-839.
8. Keijzer, Marleen, Willem M. Star, and Pascal RM Storchi. "Optical diffusion in layered media." *Applied Optics* 27.9 (1988): 1820-1824.
9. Ishimaru, Akira. "Diffusion of light in turbid material." *Applied optics* 28.12 (1989): 2210-2215.
10. Meglinski, Igor V., and Stephen J. Matcher. "Quantitative assessment of skin layers absorption and skin reflectance spectra simulation in the visible and near-infrared spectral regions." *Physiological measurement* 23.4 (2002): 741.
11. Beauvoit B, Evans S M, Jenkins T W, Miller E E and Chance B 1995 Correlation between the light scattering and themitochondrial content of normal tissues and transplantable rodent tumorsAnal. Biochem.226167–7
12. Wilson J D, Cottrell W J and Foster T H 2007 Index-of-refraction-dependent subcellular light scattering observedwith organelle-specific dyesJ. Biomed. Opt.12014010
13. aidi I S, Jacques S L and Tittel F K 1995 Mie and Rayleigh modeling of visible-light scattering in neonatal skin
14. Groenhuis, R. A. J., Hedzer A. Ferwerda, and J. J. Ten Bosch. "Scattering and absorption of turbid materials determined from reflection measurements. 1: Theory." *Applied optics* 22.16 (1983): 2456-2462.
15. Kneen, Malea, et al. "Green fluorescent protein as a noninvasive intracellular pH indicator." *Biophysical journal* 74.3 (1998): 1591-1599.
16. Yang, Haw, et al. "Protein conformational dynamics probed by single-molecule electron transfer." *Science* 302.5643 (2003): 262-266.
17. Okabe, Kohki, et al. "Intracellular temperature mapping with a fluorescent polymeric thermometer and fluorescence lifetime imaging microscopy." *Nature communications* 3 (2012): 705.
18. Dahiya, P., et al. "Effect of protic solvents on twisted intramolecular charge transfer state formation in coumarin-152 and coumarin-481 dyes." *Chemical physics letters* 414.1-3 (2005): 148-154.
19. Alberts B, Johnson A, Lewis J, et al. Molecular Biology of the Cell. 4th edition. New York: Garland Science; 2002. Catalysis and the Use of Energy by Cells. Available from: https://www.ncbi.nlm.nih.gov/books/NBK26838/
20. Blacker, Thomas S., et al. "Separating NADH and NADPH fluorescence in live cells and tissues using FLIM." *Nature communications* 5 (2014): 3936.
21. Monici, Monica. "Cell and tissue autofluorescence research and diagnostic applications." *Biotechnology annual review* 11 (2005): 227-256.
22. Kienle, Alwin, et al. "Spatially resolved absolute diffuse reflectance measurements for noninvasive determination of the optical scattering and absorption coefficients of biological tissue." *Applied optics* 35.13 (1996): 2304-2314.

23. Yaroslavsky, A. N., et al. "Optical properties of selected native and coagulated human brain tissues in vitro in the visible and near infrared spectral range." *Physics in Medicine & Biology* 47.12 (2002): 2059.
24. Svensson, Tomas, et al. "Characterization of normal breast tissue heterogeneity using time-resolved near-infrared spectroscopy." *Physics in Medicine & Biology* 50.11 (2005): 2559.
25. Patterson, Michael S., Britton Chance, and Brian C. Wilson. "Time resolved reflectance and transmittance for the noninvasive measurement of tissue optical properties." *Applied optics* 28.12 (1989): 2331-2336.
26. Abdlaty, Ramy, et al. "Hyperspectral imaging: comparison of acousto-optic and liquid crystal tunable filters." *Medical Imaging 2018: Physics of Medical Imaging*. Vol. 10573. International Society for Optics and Photonics, 2018.
27. Morris, Hannah R., Clifford C. Hoyt, and Patrick J. Treado. "Imaging spectrometers for fluorescence and Raman microscopy: acousto-optic and liquid crystal tunable filters." *Applied spectroscopy* 48.7 (1994): 857-866.
28. Becker, Wolfgang, et al. "High resolution TCSPC lifetime imaging." *Multiphoton Microscopy in the Biomedical Sciences III*. Vol. 4963. International Society for Optics and Photonics, 2003.
29. Requejo-Isidro, J., et al. "High-speed wide-field time-gated endoscopic fluorescence-lifetime imaging." *Optics letters* 29.19 (2004): 2249-2251.
30. Gadella, Theodorus WJ, Arie van Hoek, and Antonie JWG Visser. "Construction and characterization of a frequency-domain fluorescence lifetime imaging microscopy system." *Journal of fluorescence* 7.1 (1997): 35-43
31. Rajaram, Narasimhan, Tri Nguyen, and James W. Tunnell. "Lookup table–based inverse model for determining optical properties of turbid media." *Journal of biomedical optics* 13.5 (2008): 050501.
32. Farrell, Thomas J., Michael S. Patterson, and Brian Wilson. "A diffusion theory model of spatially resolved, steady-state diffuse reflectance for the noninvasive determination of tissue optical properties in vivo." *Medical physics* 19.4 (1992): 879-888.
33. Ballew, Richard M., and J. N. Demas. "An error analysis of the rapid lifetime determination method for the evaluation of single exponential decays." *Analytical Chemistry* 61.1 (1989): 30-33.
34. Li, Day-Uei, et al. "Hardware implementation algorithm and error analysis of high-speed fluorescence lifetime sensing systems using center-of-mass method." *Journal of biomedical optics* 15.1 (2010): 017006.
35. Weber, Gregorio. "Resolution of the fluorescence lifetimes in a heterogeneous system by phase and modulation measurements." *The Journal of Physical Chemistry* 85.8 (1981): 949-953.
36. Digman, Michelle A., et al. "The phasor approach to fluorescence lifetime imaging analysis." *Biophysical journal* 94.2 (2008): L14-L16.
37. Martelo, Liliana, Alexander Fedorov, and Mário N. Berberan-Santos. "Fluorescence phasor plots using time domain data: effect of the instrument response function." *The Journal of Physical Chemistry B* 119.32 (2015): 10267-10274.
38. Jo, Javier A., et al. "Fast model-free deconvolution of fluorescence decay for analysis of biological systems." *Journal of Biomedical Optics* 9.4 (2004): 743-753.
39. Yuan, Mengtao, et al. "Use of discrete Laguerre sequences to extrapolate wide-band response from early-time and low-frequency data." *IEEE transactions on microwave theory and techniques* 52.7 (2004): 1740-1750.
40. Žukauskas, A., et al. "Characterization of biological materials by frequency-domain fluorescence lifetime measurements using ultraviolet light-emitting diodes." Optical Materials 30.5 (2008): 800-805.
41. Berezin, Mikhail Y., and Samuel Achilefu. "Fluorescence lifetime measurements and biological imaging." Chemical reviews 110.5 (2010): 2641-2684.
42. International Commission on Non-Ionizing Radiation Protection. "Guidelines on limits of exposure to ultraviolet radiation of wavelengths between 180 nm and 400 nm (incoherent optical radiation)." Health Physics 87.2 (2004): 171-186.
43. Ramanujam, Nirmala, et al. "Cervical precancer detection using a multivariate statistical algorithm based on laser-induced fluorescence spectra at multiple excitation wavelengths." Photochemistry and Photobiology 64.4 (1996): 720-735.

44. Bydlon, Torre M., et al. "Chromophore based analyses of steady-state diffuse reflectance spectroscopy: current status and perspectives for clinical adoption." *Journal of biophotonics* 8.1-2 (2015): 9-24.
45. Hinni, Michael L., et al. "Surgical margins in head and neck cancer: a contemporary review." Head & neck 35.9 (2013): 1362-1370.
46. Kristoffersen, Arne S., et al. "Testing fluorescence lifetime standards using two-photon excitation and time-domain instrumentation: rhodamine B, coumarin 6 and lucifer yellow." Journal of fluorescence 24.4 (2014): 1015-1024.
47. Papaioannou, Thanassis, et al. "Effects of fiber-optic probe design and probe-to-target distance on diffuse reflectance measurements of turbid media: an experimental and computational study at 337 nm." Applied Optics 43.14 (2004): 2846-2860.
48. Cappon, Derek, et al. "Fiber-optic probe design and optical property recovery algorithm for optical biopsy of brain tissue." Journal of biomedical optics 18.10 (2013): 107004.
49. Marmarelis, Vasilis Z. "Identification of nonlinear biological systems using Laguerre expansions of kernels." *Annals of biomedical engineering* 21.6 (1993): 573-589.
50. Janssens, Luc D., et al. "A systematic study of the global analysis of multiexponential fluorescence decay surfaces using reference convolution." *Journal of physical chemistry* 94.9 (1990): 3564-3576.
51. Ranjit, Suman, et al. "Fit-free analysis of fluorescence lifetime imaging data using the phasor approach." *Nature protocols* 13.9 (2018): 1979.
52. Nie, Z. (2014) Integration of time-resolved fluorescence and diffuse reflectance spectroscopy for intraoperative detection of brain tumor margin (doctoral dissertation), McMaster University, Ontario, Canada
53. DaCosta, Ralph S., Helene Andersson, and Brian C. Wilson. "Molecular Fluorescence Excitation–Emission Matrices Relevant to Tissue Spectroscopy¶." *Photochemistry and photobiology* 78.4 (2003): 384-392.